Variation of snow mass in a regional climate model simulation covering the Tianshan Mountains, Central Asia

Tao Yang[1,2,3,4,5,6], Qian Li[1,2,7], Xi Chen[1,3,5,7*], Rafiq Hamdi [8], Philippe De Maeyer[4,5,6,9] and Lanhai Li[1,2,3,7,10*]

[1] State Key Laboratory of Desert and Oasis Ecology, Xinjiang Institute of Ecology and Geography, Chinese Academy of Sciences, Urumqi 830011, China;

[2] Ili Station for Watershed Ecosystem Research, Chinese Academy of Sciences, Xinyuan 835800, China;

[3] University of Chinese Academy of Sciences, Beijing 100049, China;

[4] Department of Geography, Ghent University, 9000 Ghent, Belgium;

[5] Sino-Belgian Joint Laboratory of Geo-information, Urumqi 830011, China;

[6] Sino-Belgian Joint Laboratory of Geo-information, 9000 Ghent, Belgium;

[7] CAS Research Centre for Ecology and Environment of Central Asia, Urumqi 830011, China;

[8] Meteorological and Climatological Department, Royal Meteorological Institute, Brussels, Belgium;

[9] Xinjiang Institute of Ecology and Geography, Chinese Academy of Sciences, Urumqi 830011, China;

[10] Xinjiang Key Laboratory of Water Cycle and Utilization in Arid Zone, Urumqi 830011, China.

*****Correspondence: chenxi@ms.xjb.ac.cn; lilh@ms.xjb.ac.cn Tel: +86-991-7823125

Key Point:

1. Compared with the ERA5 dataset, the optimizing WRF/Noah-MP reduced by 95.74% RMSE and 93.02% MB of the snow depth estimation, respectively.
2. The climatological March snow mass measured 97.85 (±16.60) gigatonnes in the Tianshan Mountains and exhibited a negligible tendency.
3. The total precipitation during the cold season controlled the variation of the March snow mass.

Abstract:

Mountain snow is a fundamental freshwater supply in the arid regions. Climate warming alters the timing of snowmelt and shortens the snow cover duration, which profoundly influences the regional climate and water management. However, a reliable estimation of snow mass in the Tianshan Mountains (TS) is still unclear due to the scarcity of extensive continuous surface observations and a complex spatial heterogeneity. Therefore, a long-time series of snow simulation was performed in the WRF/Noah-MP from 1982 until 2018 to quantify the snow mass in the TS, forced by the ERA5 reanalysis data and real-time updated leaf area index and green vegetation fraction. Meanwhile, March snow mass (close to the annual peak snow mass), snow cover fraction (SCF), and trends were investigated in the TS. The results indicated a good accuracy of the estimated snow water equivalent (root mean square error (RMSE): 7.82 mm/day) with a slight overestimation (2.84 mm/day). Compared with the ERA5 dataset, the RMSE and mean bias (MB) of the daily snow depth from the WRF/Noah-MP were significantly reduced by 95.74% and 93.02%, respectively. The climatological March snow mass measured 97.85 (±16.60) gigatonnes in the TS and exhibited a negligible tendency. The total precipitation during the cold season controlled the variations of the March snow mass. The increased precipitation in the high-altitude regions contributed to an extensive snow mass, which could offset the loss in the TS lowland. In contrast, rapidly rising air temperature caused a significant reduction of the March SCF, particularly in the Southern TS.

Key Words: WRF/Noah-MP, snow mass, snow depth, snow water equivalent, ERA5, vegetation parameters

1. Introduction

The seasonal snowpack plays an essential role in the water resources budget of the global mountainous area and provides freshwater supply for over 1/6 of the world's population (Barnett et al., 2005; Huning & AghaKouchak, 2020), which has a profound effect on the food production of irrigated agriculture and snowmelt runoff regimes in the snow-dominated basin (Qin et al., 2020). It also strongly affects regional climate system, alpine phenology, and biogeochemical processes through regulation of the land-atmospheric exchanges of water and energy (Arndt et al., 2020; Tomaszewska et al., 2020; Zhang, 2005). In addition, snow attracts recreational activities and is an important resource of winter

tourism (Deng et al., 2019), but it also causes snow-related disasters, such as snow avalanches and snowmelt flooding (Ballesteros-Cánovas et al., 2018; Schweizer et al., 2003). Despite the fact that snow provides crucial freshwater resources for agricultural practices and ecosystem services, present approaches show a large uncertainty regarding the snow mass estimation in a global mountainous area due to the presence of orographic barriers, its strong vertical and horizontal variability, diverse vegetation cover, and representative sites for snow measurement (Dong, 2018; Dozier et al., 2016; Mudryk et al., 2015). The accuracy of the snow mass map based on the in-situ observations interpolation depends on the number and representative of the ground observations, while a sparse network of snow observations usually exists in the mountainous environment, especially in the area with dense vegetation and a complex topography (Dozier et al., 2016; Mortimer et al., 2020). The passive microwave sensors could provide a nearly real-time global snow mass estimation by means of the algorithms of microwave brightness temperatures, but a poor performance was reported in the presence of forest, wet snow, deep snow, and large snow grains (Che et al., 2016; Takala et al., 2011). Notably, most gridded snow water equivalent (SWE) products from passive microwave instruments exclude the alpine area or exhibit an underestimation (Bormann et al., 2018; Pulliainen et al., 2020; Takala et al., 2011). The sensor's inconsistencies from different passive microwave platforms might lead to uncertainty in the detected trends of long-time snow mass products (Smith & Bookhagen, 2016). Moreover, a further improvement of the snow mass estimation in passive microwave measurements (~25km) and global reanalysis datasets (>30 km) is restricted in the mountainous regions with a large varying heterogeneity of snow physical characteristics due to the coarse spatial resolution (Daloz et al., 2020), and tend to be underestimated (Mudryk et al., 2015; Wrzesien et al., 2019). In contrast, although the active microwave remote sensing has been used to retrieve the snow mass with a finer spatial resolution (Lievens et al., 2019), the low accuracy is caused by the repeat-pass interval and a complex underlying surface (Dong, 2018). Similarity, the large-scale application of continuous snow mass measurements from the Unmanned Aerial Vehicles and airborne LiDAR is limited by flight time and sight (Dozier et al., 2016). Furthermore, the snow physical module within the land surface models (LSMs) has a large potential to estimate the snow processes on the complex terrain (Holtzman et al., 2020; Wrzesien et al., 2018), but a lack of both accurate forcing data and multi-parameters calibration constraints its application in the snow mass estimation of mountainous areas (Pritchard et al., 2020; Ryken et al., 2020).

The land surface-atmosphere coupling in regional climate models (RCMs), such as the Weather Research and Forecasting (WRF) model (Skamarock et al. 2008), could precisely estimate the snow mass in mountainous regions by reproducing correctly the orographic precipitation at a high spatial resolution (S. Chen et al., 2019; Minder et al., 2016; Wrzesien et al., 2017). More specifically, the advanced model structures and parameterization schemes in the RCM LSMs, such as the sophisticated microphysics schemes, the multilayer snowpack and separate vegetation canopy model have been proven to produce a reasonable snowfall estimation and snow-related water-heat exchange processes (X. Cai et al., 2014; Niu et al., 2011; Tomasi et al., 2017). Indeed, as the typically third-generation LSM, the Noah LSM with Multiparameterization Options (Noah-MP) model (Niu et al., 2011) within the WRF has a better ability to describe the snow processes in a mixed forest cover and complex terrain environment compared with in-situ and remote sensing observations, particularly in the snow ablation season (Liu et al., 2019; Musselman et al., 2018; Wrzesien et al., 2019). Since most land surface parameters of snow process in the Noah-MP model are obtained from the look-up table, coarse gridded datasets and empirical formulas, which could not fully capture the heterogeneity of the snowpack characteristics in the extensive mountains (Jiang et al., 2020; You, Huang, Yang, et al., 2020). For example, the vegetation parameters, such as the leaf area index (LAI) and green vegetation fraction (FVC) are determined by vegetation types or prescribed from climatological datasets with no real-time update, which trigger large uncertainties in the snow mass estimation (Kumar et al., 2019; Tomasi et al., 2017). More realistic vegetation parameters and schemes exhibited a more accurate snow characteristics estimation in the LSMs (Kumar et al., 2019; T. Yang et al., 2020), particularly in the dense vegetation regions through the improvement of interception, sublimation and melting in the snow accumulation and ablation period (Helbig et al., 2019; Niu & Yang, 2004). Due to the limitation of computing time, the snow simulation in the RCM LSMs often runs a relatively short period, which could not reveal the long-time variation of mountainous snow (Oaida et al., 2015; Wrzesien et al., 2019). Additionally, the performance of the snow mass estimation in the RCM LSMs heavily depends on the accuracy of the reanalysis forcing data (Liu et al., 2019; Terzago et al., 2020; Yan Wang, Xie, et al., 2020). The ERA5 is the fifth-generation global reanalysis product released from the European Centre for Medium-range Weather Forecasts (ECMWF) and has assimilated more observations with a higher spatiotemporal resolution compared with the widely used ERA-Interim reanalysis (Copernicus Climate Change Service (C3S), 2017; Hersbach et al., 2020). Hence, it is expected that a reliable long-time series

of snow datasets could be obtained from the RCM LSMs in poorly gauged mountainous regions forced by more accurate reanalysis data and updated vegetation parameters.

Having the function of both the ecological barrier and water tower of Central Asia, the Tianshan Mountains (TS) are located in the hinterland of the Eurasian arid regions (Farinotti et al., 2015). The glaciers/snowmelt water provide a large proportion of recharge supply for the main surface runoffs (Sorg et al., 2012), which is the base freshwater source for the regional mountain-oasis-desert system (Y. Chen et al., 2018). An accurate snow mass estimation and variations significantly affect the surrounding irrigated agriculture, ecosystem services and water resources management (Unger-Shayesteh et al., 2013; T. Yang, Li, Ahmad, et al., 2019). The steep terrain, mixed land cover, and diverse climate systems produce a significantly heterogeneous snow mass pattern (E. M. Aizen et al., 2001; J. W. Yang et al., 2020). Unfortunately, the majority of the snow studies focused on the variations in snow cover and snow depth (SD) in a partial or entire TS utilizing point-scale in-situ observations and remote sensing measurements due to the limitation of sparse observations and a complex terrain (Q. Li et al., 2019; Tomaszewska & Henebry, 2018). Both the observations from the meteorological stations and the passive microwave sensors demonstrated that the snow end date significantly advanced in the TS during the past decades due to climate warming (Q. Li et al., 2019; N. Ma et al., 2020; T. Yang, Li, Ahmad, et al., 2019). Moreover, the field observations suggested that the snow characteristics in the forest regions are significantly distinguishable from other land cover types (Dai et al., 2012; Lu et al., 2017). Recently, the short time snow simulations on the SD and SWE have been well performed using the offline Noah-MP and WRF/Noah-MP on a point scale and regional scale, respectively (T. Yang et al., 2020; You, Huang, Gu, et al., 2020; You, Huang, Yang, et al., 2020). However, as the most important quantity indicator representing the regional snow resources, the snow mass and its long-time variations under a warming trend are still unclear in the entire TS due to the scarcity of accurate observation datasets.

The study aims to quantify the snow mass and its variations in the entire TS from 1982 till 2018 by means of the WRF/Noah-MP, which was forced by a new generation of reanalysis datasets (ERA5) and real-time updated vegetation parameters (LAI and FVC). The specific objectives are: (1) to evaluate the performance of a long-time snow mass estimation in the WRF/Noah-MP; (2) to investigate the spatiotemporal variability of the snow mass and snow cover fraction (SCF); (3) to identify possible causes and implications of the model uncertainty and snow variations. This is the first attempt to

quantify the snow storage and its variations in the entire TS. The results will enhance the understanding of the regional snow resources and will provide a fundamental dataset for the regional studies on the cryospheric, hydrological, and environmental processes.

2. Data and methods

2.1 Study area

As the largest mountain system in Central Asia, the TS are located at 67°-95°E and 39°-46°N, stretching over 2500 km from west to east, 250-350 km from south to north, and covering over 800,000 km^2 (Figure 1b). The average height of the TS measures about 4,000 m above sea level (a.s.l.). Affected by the westerlies and the complex topography, the TS exhibit a distinct gradient of continentality with an increasing temperature and precipitation from southeast to northwest (Figures 1c and 1d). The total average annual precipitation and mean temperature in the entire TS amount to 329.3 mm and 4.6°C, respectively (T. Yang, Li, Ahmad, et al., 2019). Approximately 1/3 of the total precipitation (500-700 mm) occurs as the snowfall in the northern slope of the TS (Guo & Li, 2015). Grassland is the dominating land cover type (T. Yang et al., 2020) and the forest cover prevails between 1,300 and 2, 800 m a.s.l. (Lu et al., 2017). Both the Western TS (WTS) and Northern TS (NTS) have a relatively moist climate, while the Eastern TS (ETS) and Southern TS (STS) exhibit a typically continental climate (V. B. Aizen et al., 1997; Sorg et al., 2012). In addition, the precipitation in the ETS and NTS concentrates during spring and early summer, which is later than the WTS (later winter to early spring) but earlier in the STS (summer) (Sorg et al., 2012). Abundant precipitation in the mountainous area shapes the “wet island” landscape and contributes to the rich snow and glaciers resources, which has a significant impact on the growth of the regional irrigated agriculture and industry (Farinotti et al., 2015).

Figure 1

2.2 Datasets acquisition and processing

2.2.1 Ground surface data

The China Meteorological Administration (CMA) and the Tianshan Station for Snow Cover and Avalanche Research (TSSAR), Chinese Academy of Sciences provided 56 meteorological stations in the

target area (Figure 1b), which includes the mean daily temperature, SD, precipitation and 5-day SWE (when SD > 5cm). In addition, All-Russian Research Institute of Hydrometeorological Information-World Data Centre (RIHMI-WDC) provided 4 stations with daily SD observations. The stations were collected from the National Snow and Ice Data Centre (NSIDC). After exclusion of the stations with over 10% missing data, 54 stations have been processed for the monthly precipitation and mean temperature, respectively. Detailed information was shown in Table1.

Table 1

2.2.2 Remote sensing product

The variation in the Terrestrial Water Storage (TWS) during the cold season is mainly caused by the snow evolution in the mountainous regions (Wrzesien et al., 2018). The Noah-MP treats the TWS as the sum of the SWE, soil moisture contents, groundwater storage, and canopy water contents (Kumar et al., 2019). Due to a lack of in-situ observations in the alpine region, the Gravity Recovery and Climate Experiment (GRACE) of the monthly TWS anomaly product (version RL06) at a 0.5° spatial resolution was applied so as to compare it with the modeled TWS. In addition, the Moderate Resolution Imaging Spectroradiometer Satellite (MODIS) monthly SCF in the Climate Modeling Grid (MOD10CM) product at a 0.05° spatial resolution was used in order to evaluate the estimated SCF.

The WRF adapted the basis land cover (LC) containing the 2000 global annual LC map at a 300 m spatial resolution which was produced by the European Space Agency (ESA) Climate Change Initiative (CCI) project (https://www.esa-landcover-cci.org/). The CCI-LC product includes the annual global land cover map from 1992 to 2018 with an overall accuracy of 75.4 % (ESA, 2017). According to Huang et al., 2020, the CCI-LC2000 was converted into the MODIS-20 category as WRF LC. As the key vegetation parameters, the 8-day LAI and FVC products at a 0.05° spatial resolution from 1982-09-01 till 2018-09-30 have been obtained from the Global Land Surface Satellite (GLASS) products (http://glass.umd.edu/index.html), manufactured by the Advanced Very High-Resolution Radiometer (AVHRR) reflectance datasets (Xiao et al., 2016). Compared with the other global vegetation datasets, the GLASS LAI and FVC data have been successfully applied to the land-atmosphere interaction simulation, due to the higher quality (Fang et al., 2019; Xiao et al., 2014). The 8-day GLASS

LAI and FVC datasets were linearly interpolated to a daily scale at a 9 km resolution so that the real-time updates the LAI and FVC in the WRF/Noah-MP.

2.3 Model configuration

In this study, the WRF-AWR 4.01 coupled with the Noah-MP (Niu et al., 2011) model was used for the snowpack simulation in the TS and performed from September 1982 until September 2018. The model was initialized at 00:00 UTC on September, 1st each year and terminated on September, 30th the next year. The initial September output was discarded as a model spin-up (Jesse Norris et al., 2018), hence the 36 full cold seasons (from November to March) retained output. Previous studies demonstrated that a grid resolution of smaller than 10 km could reveal the realistic orographic precipitation processes in the complex topography (J. Norris et al., 2015; Wrzesien et al., 2018). Considering the limited storage space and computing timing, the WRF was configured with the one-way double nested domains along with 35 vertical levels from the surface top to 50 hPa (Figure 1a). The outer domain (D01, 27 km grid spacing) had 317 × 145 grids in the west-east and south-north direction, and the inner domain (D02, 9 km grid spacing) was nested with 304 × 133 grids. As the updated version of the ERA-Interim reanalysis dataset, the ERA5 reanalysis (Hersbach et al., 2020) from the European Centre for Medium-Range Weather Forecasts (ECMWF) has proven to perform very well in the hydrological applications and regional climate downscaling (Nogueira, 2020; Ou et al., 2020). Therefore, the ERA5 (31 × 31km) reanalysis dataset updated in a 6-hourly interval has been chosen as the initial and lateral boundary conditions for D01 and D02 (https://cds.climate.copernicus.eu/cdsapp#!/home), as well as the sea surface temperature. The main parameterization schemes were exposed in Table 2 (T. Yang et al., 2020): the Single-Moment 6-Class (WSM-6) cloud microphysical scheme (S. Hong & Lim, 2006), Rapid Radiation Transfer (RRTM) longwave radiation model (Mlawer et al., 1997), Yonsei University planetary boundary layer (YSU) (S. Y. Hong et al., 2006), Kain-Fritsch Cumulus Scheme (Kain, 2004), Dudhia shortwave radiation model (Dudhia, 1989), MM5 Monin-Obukhov surface layer (Monin & Obukhov, 1959) and Noah-MP Land Surface (Niu et al., 2011).

Table 2

As an advanced version of the Noah land surface model, the Noah-MP model provides multiple parameterization options for the land-atmosphere interaction process simulations (Niu et al., 2011). The three-layer snow structure could effectively describe the processes of liquid water contents, snow

231 destructive/melt metamorphism, and compaction in the snowpack. The key physical parameterization
232 schemes in the Noah-MP including (Niu et al., 2011): the CLASS (Canadian Land Surface Scheme)
233 ground surface albedo, Jordan's scheme for precipitation partitioning between snow and rain (Jordan,
234 1991), thermal conductivity function considering the snow density, Monin-Obukhov surface layer drag
235 coefficient, snow canopy interception and upload with the effect of phase change, temperature and wind
236 (Niu & Yang, 2004), the Ball-Berry vegetation stomatal resistance, the Noah semi-implicit snow/soil
237 temperature scheme, and two-streams approximation of the radiative transfer scheme with a
238 consideration of the canopy gap probability for the vegetation shading and scattering (R. Yang et al.,
239 2001). The look-up table, remote sensing dataset and prediction based on the carbon budgets provide
240 different options of LAI and FVC for the dynamic vegetation model, which has a significant influence on
241 the snow interception and energy exchange (Gan et al., 2019). The default vegetation parameters'
242 look-up table and LC data showed large uncertainties in the climate simulations (Bonekamp et al., 2018).
243 Therefore, the CCI-LC 2000 was selected to deliver land cover data input for both D01 and D02 in this
244 study. In addition, the daily GLASS LAI and FVC data were updated real-time in D02 for the Noah-MP
245 model. The LAI and FVC have utilized the default geographical dataset for D01.

246 2.3 Snow mass calculation

247 The March snow is the closest to the annual peak snow mass in the TS (Figure 2). In addition, as the
248 transitional season of the snowpack, March plays a significant role in the snow accumulation and
249 ablation (Pulliainen et al., 2020; Ye, 2019). The snow mass (gigatonnes, Gt) in the whole TS could be
250 calculated as follows:

251 $$Snow\ mass = \sum_{i=1}^{N} \frac{81 \times 10^3 \times SWE_i}{10^9} \quad (1)$$

252 where N is the total number of the WRF grid cells in the TS and SWE_i represents the March SWE
253 estimated by the WRF/Noah-MP in the i^{th} grid cell.

254 **Figure2**

255 2.4 Evaluation method and trend analysis

The trend slope and its significant level of climate variables were calculated by the Sen method (Sen, 1968) and the Mann-Kendall (M-K) trend test (Mann, 1945; Kendall, 1975), respectively. The T2, SD, precipitation, and SWE values from the nearest grid point of the WRF output were compared with the in-situ observations. The performance of the WRF estimation was evaluated by relevant observations based on metrics: the Correlation coefficient (R), Mean bias (MB), and Root Mean Square Error (RMSE).

$$R = \frac{\sum_{i=1}^{N}\left[\left(Sim(i)-Sim_{mean}\right)\left(Obs(i)-Obs_{mean}\right)\right]}{\sqrt{\sum_{i=1}^{N}\left(Sim(i)-Sim_{mean}\right)^2\sum_{i=1}^{N}\left(Obs(i)-Obs_{mean}\right)^2}} \quad (2)$$

$$MB = \frac{1}{N}\sum_{i=1}^{N}(Sim(i)-Obs(i)) \quad (3)$$

$$RMSE = \sqrt{\frac{1}{N}\sum_{i=1}^{N}(Sim(i)-Obs(i))^2} \quad (4)$$

where N demonstrates the total number of the observed or simulated data, $Sim(i)$ and $Obs(i)$ represent the simulated and observed values at the timestep i, respectively, and Sim_{mean} and Obs_{mean} illustrate the mean of the simulated and observed values, respectively.

3 Results

3.3 Performance of the long-time snow simulation

3.3.1 SD and SWE

The performance of the snow simulation in the WRF/Noah-MP is shown in Figures 3-5. Generally, the SD and SWE simulations averaged from all stations in D02, which exhibited the highest accuracy compared to D01 and ERA5 (Figure 3a). In addition, a slight overestimation of the SD and SWE was found in D01, D02, and ERA5 compared with the in-situ observations (Figures 4a and 4b). Compared with the ERA5 (RMSE: 3.64 cm/day and MB: 2.10 cm/day), the daily SD simulation in D01 and D02 could effectively reduce the RMSE (2.78 and 1.86 cm/day, respectively) and MB (1.32 and 0.15 cm/day, respectively). The D01, D02 and ERA5 showed a consistent spatial pattern of RMSE and MB in the SD simulations (Figures 5a-f). Large RMSE values of SD simulations were observed in the

high-altitude regions (a.s.l. >3000 m) of TS (Figures 2b). The RMSE values in the low-altitude regions (a.s.l. <1500 m) of STS were significantly smaller than in the NTS and ETS (Figures 4a, 4c, and 4e). Similarly, large MB values of all SD simulations were displayed in the high-altitude regions of TS with a significant overestimation (Figure 3c). A widespread slight overestimation of all SD simulations prevailed in the low-altitude regions of the STS and eastern ETS. It was noted that a consistent underestimation of the SD simulation was seen in the Ili Valley and at the intersection of the NTS and ETS (Figures 4c-d and 4f).

Figure 3

Figure 4.

Figure 5

3.3.2 TWS and SCF

Most of the in-situ observations are located in the low-altitude regions are characterized by a sparse and uneven distribution. Hence, the monthly TWS anomaly and SCF from the WRF/Noah-MP estimation in the TS were evaluated by the GRACE TWS and MODIS SCF products during the cold season (Figures 4c-d and 6a-b). The monthly TWS anomaly from WRF/Noah-MP demonstrated a good shape as compared with GRACE TWS (Figure 4c). Although the TWS simulation showed a general overestimation in WRF/Noah-MP (Table 3), a significant underestimation was noticed after 2012/2013. Compared with MODIS, the monthly SCF illustrated high accuracy in the WRF/Noah-MP estimation of the TS but an overestimation was also seen during the cold season (Figure 4d and Table 3). The snow-covered area in the WRF/Noah-MP was significantly larger than that in the MODIS observations, especially the Tarim Basin (Figures 6a-b). The high SCF (exceeding 90 %) area additionally enlarged in the high-mountain regions.

Figure 6

Table 3

3.4 Spatiotemporal variability of the snow mass and SCF

3.4.1 Spatiotemporal variability of the maximum SD and SWE

The spatial distribution of the maximum SD and SWE in the TS during the cold season is shown in Figure 7. These increased from east to west, and from south to north (Figures 7a-c). The maximum SD values exceeded 80 cm in the WTS and high-altitude regions of the Ili Valley, whose maximum SWE values reached 250 mm, correspondingly. Most TS regions experienced an rise in the maximum SWE except the low-altitude regions of the STS and WTS (Figure 7d). In particular, a significant augmentation of the maximum SWE was noticed in the ETS and Pamir regions.

Figure 7

3.4.2 Spatiotemporal variability of the snow mass

The patterns and trends of the mean March snow mass estimated by the WRF/Noah-MP across the TS are presented in Figure 8. The estimation indicated that the March snow mass in the TS amounted to 97.85 (±16.60) Gt (mean SWE 112.21 mm) with a negligible trend (Figure 8a). The mean March snow mass in the WTS (64.29 ±11.40 Gt) was significantly larger than in the NTS (21.45 ±5.09 Gt), ETS (2.75 ±0.8 Gt) and STS (9.36 ±1.64 Gt) (Figure 7c). In addition, the March snow mass consistently exhibited insignificant changes in all TS sub-regions during the past 36 years. However, the March SWE showed an opposite trend between the high-altitude and low-altitude regions (Figures 8b and 8d). The March SWE almost showed a decrease in the low-altitude regions (below 2,500 m) of the TS (Figure 8b), and the significantly decreasing values prevailed in the STS (Figure 8d). In contrast, the March SWE experienced a rising trend in the high-altitude regions (over 3,000 m), especially in the near Pamir regions. Notably, the highest elevation zone with a decreasing March SWE could reach 3,000-3,500 m in the STS, which was higher than other sub-regions (between 2,500 and 3,000 m).

Figure 8

3.4.3 Spatiotemporal variability of the SCF

The variation of the SCF in the transition season is sensitive. The spatial changes of the mean SCF during the cold season, November, and March from 1982 to 2018 were displayed in Figure 9. The SCF experienced a decreasing trend during the cold season, especially in March, showing a significant decrease (Figure 9a and Table 4). The decreasing rate of the mean SCF in November was smaller than in March, but larger than the cold season. The trend of the mean SCF during the cold season and

November showed a similar distribution pattern (Figures 9b-d). The significantly decreasing values of the SCF during the cold season and November were sporadically found in the eastern STS and the high-altitude regions of the Ili Valley. Additionally, the low-altitude regions of the WTS also demonstrated a significant decrease in the mean SCF during the cold season. By contrast, a significantly large decrease in the March SCF was to be found in the low-altitude regions of the TS. Particularly for the ETS and STS, the decreasing rate of the March SCF exceeded 6% per decade.

Figure 9

Table 4

4 Discussion

4.1 Influencing factors of the snow simulation performance in WRF/Noah-MP

The snow model performance is highly sensitive to the accuracy of the meteorological forcing data in a mountainous environment (Terzago et al., 2020). The high-quality of the simulated precipitation and temperature could reduce the uncertainty of the snow simulation in the RCM LSMs (Liu et al., 2019; Wrzesien et al., 2019), especially in the mountainous zone with dense forest. Reasonable precipitation could be reproduced by the WRF dynamical downscaling in the complex terrain with a fine spatial resolution. Thus, compared with the original ERA5 dataset and D01, the RMSE of the daily SD in D02 was reduced significantly by 95.74% and 49.12%, respectively (Figure 3). The coarse-resolution global reanalysis products and GlobSnow passive microwave SWE series' products failed to reveal the sub-grid snow characteristics of the alpine regions (Bormann et al., 2018; Dozier et al., 2016). Previous studies reported that the near-surface air temperature in ERA5 reduced the cold bias compared with the ERA-Interim (Hersbach et al., 2020; C. Wang et al., 2019), but a general cold bias could still be noticed in the dynamic downscaling results of the TS (Figures 10a and 10c), particularly in the STS. In addition, an underestimation of the total precipitation during the cold season prevailed in the intersection between the NTS and ETS, and the low-altitude regions of the WTS and STS (Figure 9b and 9d), but overestimated values were seen in the high-altitude regions, which were consistent with the performance from the WRF downscaling in the Qinghai-Tibet Plateau and the original ERA5 dataset (Ou et al., 2020). Hence, an underestimation of the total precipitation caused a negative SD bias in the Ili Valley and at the intersection between the NTS and ETS (Figure 5c).

Notably, smaller SD bias values in D02 were found in the Ili Valley and the northern slope of the TS as compared with the ERA-Interim dynamic downscaling results because more precipitation was produced throughout the ERA5 dynamical downscaling in these regions (S. Chen et al., 2019; T. Yang et al., 2020). Moreover, more precipitation contributed to a reduction of the negative snow mass bias in the global mountainous area (Wrzesien et al., 2019). In contrast, the large SD deviation in the high-altitude region was mainly caused by the severely wet bias with a cold bias (Figure 5e). A severe overestimation of the ERA5 and ERA5-land SD was also reported in the Tibetan Plateau (Orsolini et al., 2019). Previous studies demonstrated that the relatively sophisticated cloud microphysics schemes, such as the Thompson microphysics scheme, performed well in the snowfall estimation on a complex terrain (J. Norris et al., 2015). Due to limited computing time resources, the WSM6 microphysics scheme might bring a large deviation in the snowfall simulation (Fernández-González et al., 2015). Although some underestimated precipitation values were found in the STS, a large cold bias was beneficial to reserve the snow and to prolong the snow cover duration (Figures 4 and 6). However, more ground snow could increase the surface albedo and aggravate the cold bias, especially in the thin snow area (W. Wang et al., 2020) (Figure 10a).

Figure 10

The physical schemes and model parameterizations have a significant influence on the snow process, particularly during the snowmelt season (You, Huang, Gu, et al., 2020). The crucial snowpack physics in Noah-MP including the snow albedo scheme considering the grain size and fresh snow, liquid water evolution in the multiple snow layers, snow density function based on the thermal conductive, turbulent flux and the moisture exchange between the canopy and snow surface, etc. (Niu et al., 2011) could effectively overcome the limitation of wet snow and forest snow in the passive microwave sensor (Dong, 2018; Dozier et al., 2016), reducing the snow mass underestimation (Wrzesien et al., 2019). The near-surface air temperature threshold is often selected as the rain-snow partitioning scheme in the most LSMs and hydrological models, but it underestimates the snowfall in the arid regions (Yuanheng Wang et al., 2019). Nevertheless, the fresh snow density is a function of the fresh snow density based on field investigation in relatively humid regions (Hedstrom & Pomeroy, 1998), but a lower one was observed in the dry TS (X. Chen et al., 2011). The underestimated vegetation emissivity scheme could

augment the interception loss and reduce the ground snow (X. Ma et al., 2019). The uncertainties mentioned above might cause a larger SD underestimation in the Ili Valley and at the intersection between the ETS and NTS (Figure 5f). The fixed fresh snow albedo parameters in most ground surface albedo schemes are designed for thick snow, but the CLASS scheme (fixed as 0.84) in the thin snow region, such as the lowland of the STS, overestimated the actual ground surface snow albedo which caused a severe cold bias and SD overestimation (W. Wang et al., 2020). Previous studies suggested that light-absorbing impurities on the snow surfaces might increase the absorption of shortwave radiation and accelerate the snowmelt (Sarangi et al., 2020). The growing aerosol contamination could change the surface albedo and enhance the snowmelt process (Barnett et al., 2005; Kang et al., 2020). Furthermore, the blowing snow causes the redistribution of the snowpack and increases the snow sublimation in dry air condition (Orsolini et al., 2019). In case these processes lack in the Noah-MP, the latter could intense the overestimation of snow in the high-altitude regions of the TS and around the Tarim Basin (Figure 5f). The soil texture dataset in WRF/Noah-MP exists in large uncertainty due to the coarse resolution and lack of sufficient field investigation (J. Li et al., 2018), which could trigger a large deviation in the land surface energy flux simulation (Jiang et al., 2020). Although the WRF reproduced well in the topographic precipitation with a 9 km spatial resolution, numerous studies revealed that a finer resolution could effectively decline the precipitation overestimation and snow simulation uncertainty on a complex terrain (Bonekamp et al., 2018; Yan Wang, Yang, et al., 2020).

The quality of the observational data might also be a source of the uncertainty in the model evaluation step (Kumar et al., 2019). Due to the wind flow, the undercatch of the snowfall in the gauge observations might contribute to excessive model precipitation in the alpine areas (Bonekamp et al., 2018). The constant human disruption such as the sensor upgrade, urban growth, and station relocation might further cause measurement errors, expanding the deviation in the model evaluation (Fiebrich et al., 2010). Due to the spatial heterogeneity on a complex terrain, a pointed-scale in-situ observation did not appear to be a robust method to evaluate the snowpack evolution in a whole grid cell (81 km^2), and the performance was up to its representative (Kumar et al., 2019; Wrzesien et al., 2018). The groundwater, lakes, glaciers, soil moisture contents are also included in the GRACE TWS (Wrzesien et al., 2018). Although the GRACE TWS anomalies were used for comparison with the TWS anomalies of the WRF/Noah-MP (Figure 4c), it could not reveal that all TWS changes were caused by the snow

417 accumulation and melting. Moreover, the gain factor, spatial resolution and systematic errors of the
418 GRACE products might result in uncertainty on the assessed result (Landerer & Swenson, 2012). It
419 was not clear that the performance of the snow simulation occurred in the WTS and high-altitude
420 regions, because most in-situ snow observations are located in the lowland of the Chinese TS area.

421 4.2 Impact of the climatic factors on the snow variability

422 Variations in precipitation, surface air temperature and atmospheric circulation regulate the snow
423 anomalies (Cohen & Jones, 2011; Zhong et al., 2018). Overall, the March snow mass showed
424 a negligible trend in the TS (Figure 3a). The passive microwave remote sensing similarly revealed a
425 low-frequency variation of snow mass in the High Mountain Asia and Eurasia but this was opposite
426 with a significant decline in North America (Pulliainen et al., 2020; Smith & Bookhagen, 2018). It was
427 noted that a change in the cold season precipitation was a dominant factor that leading to a variability
428 in the March snow mass (Table 5). Snow was more sensitive to the precipitation than the temperature
429 during the cold season in a dry-cold climate, which was consistent with the high latitude of Eurasia
430 and Central Asia (Notarnicola, 2020; Smith & Bookhagen, 2018; Zhong et al., 2018). The
431 precipitation showed a consistent increase during the cold season, particularly in the ETS and
432 high-altitude regions of the WTS and NTS (Figure 11c). In addition, a significant increase in snowfall
433 was also reported in the in-situ observations and climate model simulations (Guo & Li, 2015; de Kok
434 et al., 2020). Anthropogenic aerosols might also enhance the latent heat exchange, forming more cloud
435 and precipitation (Kang et al., 2020; Zhao et al., 2020). Meanwhile, the increased oasis expansion
436 could increase the precipitation (P. Cai et al., 2019; Piao et al., 2020).Thus, it was beneficial to
437 augment the maximum snow mass in these regions (Smith & Bookhagen, 2018) (Figure 7d). In
438 particular, a significant SWE increasing trend was identified in the regions near Pamir and the ETS
439 during winter (Smith & Bookhagen, 2018). Moreover, the heavy snowfall events happened frequently
440 (T. Yang, Li, Liu, et al., 2019), which might cause a sharp rise in SD (Zhong et al., 2018). Previous
441 studies demonstrated that the maximum SD experienced a significant increase in the Ili Valley and
442 ETS (Q. Li et al., 2019; T. Yang, Li, Liu, et al., 2019). This is however not reflected in March snow
443 mass map (Figure 8d) because the maximum snow mass was detected in the ETS during February
444 (Figure 2). The air temperature experienced an insignificant increase in the TS during the cold season
445 but exhibited a significantly rapid rise in March (Figure 11) as well as the days with a daily air

temperature > 0 °C (1.5 days per decade, $P < 0.05$). However, the air temperature measured far below 0 °C in the high-altitude regions, in which the warming trend had no obvious impact on the snowmelt. In contrast, the largely increasing March temperature could accelerate the snowmelt rate in the low-altitude regions (Figure 8b), causing more melted snow and reducing the SCF (Figure 11f). The heavy warming was strongly related to the rapid snow melting in most areas of the Northern Hemisphere in spring (Notarnicola, 2020). Nevertheless, the significantly increasing March precipitation values were seen in the TS except for the STS (Figure 11d), which might augment the snow mass and offset the snowmelt caused by the rising temperature. Furthermore, more precipitation in the snow-rain transitional season also resulted in the reduction of the snowfall verse precipitation ratio and the increased probability of rain-on-snow events (Musselman et al., 2018), which could bring more energy to the snow surface and enhance the snowmelt, advancing the snow end date and shortening the snow cover duration (Mazurkiewicz et al., 2008). This might be another reason for the significant reduction of the March SCF in the low-altitude TS regions (Figure 9d). Previous studies illustrated that the advanced snow end day was found in the lowland of the TS based on the meteorological and remote sensing observations (Q. Li et al., 2019; Notarnicola, 2020). Some evidence revealed that the variations of the El Niño–Southern Oscillation (ENSO), westerlies circulation index and North Atlantic/Arctic Oscillation (NAO, AO) have a substantial influence on the regional cold season climate as well as snow (Gerlitz et al., 2019). The strengthened mid-latitude westerlies enhance winter precipitation in the uplifted regions of the TS (Mölg et al., 2014). In addition, the interactions between the different atmospheric circulations might form heterogeneous snow trends (Smith & Bookhagen, 2018).

Figure 11

Table 5

4.3 Implications and limitations

The change in snow has an important influence on the regional climate, water resources, and ecosystems (Huning & AghaKouchak, 2020; Peng et al., 2010). The increased melted snow and the SCF decline could reduce the ground surface albedo and increase the soil moisture content (Blankinship et al., 2014), consequently, exacerbating the warming trend. The thick snow could warm

the soil surface, but the decreased snow mass would lessen the warming effect in rich snow regions and vice versa (Zhang, 2005). The increased peak SWE in the high-altitude regions may contribute to the increase in glacier mass, but a dramatic warming accelerated the glacier mass loss in the TS (Farinotti et al., 2015; Luo et al., 2013). In addition, more melted snow during the cold season (Figure 11 c) could lead to an earlier spring peak runoff and increase the risk of flooding in the snow-dominated river basin (Stewart, 2010). The shift in runoff regime might also cause a mismatch between the crop water requirements and the irrigation supply and trigger a crisis of regional water resources shortage (Qin et al., 2020). The decline in the March SCF suggested that rapid snowmelt took place during a shorter period, which easily triggered wet snow avalanches (Hao et al., 2018). Indeed, the ongoing climate warming during early spring is beneficial to snow wetting and enhances the snow avalanche risk in mountainous areas (Ballesteros-Cánovas et al., 2018). The snow mass also plays a key role in the desert vegetation growth such as ephemeral plants through a consistent soil moisture regulation until summer (Peng et al., 2010). The growth of the alpine vegetation is similarly highly sensitive to the change in snow cover (Tomaszewska et al., 2020). A longer snow cover duration could cause an earlier start of the growing season and a longer duration of the growing season, and augment the vegetation greening as a result (X. Wang et al., 2018).

Limited by the forcing data period, the variability of snow mass in this study was described during a relatively short time period. A point-scale in-situ historical snow depth reconstruction was performed based on the corrected the reanalysis data (Q. Li et al., 2018). The machine learning provided a reasonable approach so as to estimate the historical snow depth in a grid cell (J. Yang et al., 2020). In addition, the bias-correction method could significantly reduce the snow estimation uncertainty (Pulliainen et al., 2020). However, the scarcity of the surface observations gives rise to a big challenge in data assimilation and a comprehensive assessment of the snow process, especially in the altitudes exceeding 3,000 m. Thus, future work should enhance the intensive snow course observations and data assimilation in the RCM LSMs using a finer spatial resolution.

5 Conclusions

This study evaluated the performance of the snow simulation from 1982-2018 in the WRF/Noah-MP, which was forced by the ERA5 reanalysis data, real-time updated leaf area index

and green vegetation fraction, and it investigated the variability of the March snow mass and snow cover fraction in the Tianshan Mountains. The main findings of this study are described below:

1. The snow mass estimation from WRF/Noah-MP showed a high accuracy with a slight overestimation (2.84 mm/day). Compared with the ERA5, the root mean square errors and mean bias of the daily snow depth from Domain 2 were significantly reduced by 95.74% and 93.02%, respectively. However, a large uncertainty in snow estimation existed in the high-altitude regions of the Tianshan Mountains.

2. The March snow mass (97.85 ± 16.60 Gt) represented the annual maximum snow storage in the whole Tianshan Mountains. Although a widespread increase in the peak snow water equivalent was found during the cold season, the March snow mass exhibited a negligible trend. Additionally, the March snow cover fraction declined significantly, particularly in the Southern Tianshan Mountains.

3. The total precipitation during the cold season controlled the March snow mass variations as compared with the surface air temperature. The increased precipitation in the high-altitude regions contributed to the extensive snow mass, which could offset the snow mass loss in the lowland of the Tianshan Mountains under climate warming. In contrast, the significant and rapidly rising air temperature caused the March snow cover fraction reduction.

Acknowledgements

This study was supported by the projects of the National Natural Science Foundation of China (NSFC Grant No. U1703241; No. 42001061), the Strategic Priority Research Program of the Chinese Academy of Sciences, the Pan-Third Pole Environment Study for a Green Silk Road (Pan-TPE) (No. XDA2004030202) and the Chinese Academy of Sciences President's International Fellowship Initiative (PIFI, Grant No. 2017VCA0002).

References

Aizen, E. M., Aizen, V. B., Melack, J. M., Nakamura, T., & Ohta, T. (2001). Precipitation and atmospheric circulation patterns at mid-latitudes of Asia. *International Journal of Climatology*, *21*(5), 535–556. https://doi.org/10.1002/joc.626

Aizen, V. B., Aizen, E. M., Melack, J. M., & Dozier, J. (1997). Climatic and hydrologic changes in the

Tien Shan, central Asia. *Journal of Climate*, *10*(6), 1393–1404. https://doi.org/10.1175/1520-0442(1997)010<1393:CAHCIT>2.0.CO;2

Arndt, K. A., Lipson, D. A., Hashemi, J., Oechel, W. C., & Zona, D. (2020). Snow melt stimulates ecosystem respiration in Arctic ecosystems. *Global Change Biology*, *26*(9), 5042–5051. https://doi.org/10.1111/gcb.15193

Ballesteros-Cánovas, J. A., Trappmann, D., Madrigal-González, J., Eckert, N., & Stoffel, M. (2018). Climate warming enhances snow avalanche risk in the Western Himalayas. *Proceedings of the National Academy of Sciences of the United States of America*, *115*(13), 3410–3415. https://doi.org/10.1073/pnas.1716913115

Barnett, T. P., Adam, J. C., & Lettenmaier, D. P. (2005). Potential impacts of a warming climate on water availability in snow-dominated regions. *Nature*, *438*(7066), 303–309. https://doi.org/10.1038/nature04141

Blankinship, J. C., Meadows, M. W., Lucas, R. G., & Hart, S. C. (2014). Snowmelt timing alters shallow but not deep soil moisture in the Sierra Nevada. *Water Resources Research*, *50*, 1448–1456. https://doi.org/doi:10.1002/2013WR014541.

Bonekamp, P. N. J., Collier, E., & Immerzeel, W. (2018). The Impact of spatial resolution, land use, and spinup time on resolving spatial precipitation patterns in the Himalayas. *Journal of Hydrometeorology*, *19*(10), 1565–1581. https://doi.org/10.1175/JHM-D-17-0212.1

Bormann, K. J., Brown, R. D., Derksen, C., & Painter, T. H. (2018). Estimating snow-cover trends from space. *Nature Climate Change*, *8*(November), 924–936. https://doi.org/10.1038/s41558-018-0318-3

Cai, P., Hamdi, R., Luo, G., He, H., Zhang, M., Termonia, P., & De Maeyer, P. (2019). Agriculture intensification increases summer precipitation in Tianshan Mountains, China. *Atmospheric Research*, *227*(April), 140–146. https://doi.org/10.1016/j.atmosres.2019.05.005

Cai, X., Yang, Z., Xia, Y., Huang, M., Wei, H., & Leung, L. R. (2014). Assessment of simulated water balance from Noah, Noah-MP, CLM, and VIC over CONUS using the NLDAS test bed. *Journal of Geophysical Research: Atmospheres*, *119*, 1–20. https://doi.org/10.1002/2014JD022113.Received

Che, T., Dai, L., Zheng, X., Li, X., & Zhao, K. (2016). Estimation of snow depth from passive

557 microwave brightness temperature data in forest regions of northeast China. *Remote Sensing of*
558 *Environment*, *183*, 334–349. https://doi.org/10.1016/j.rse.2016.06.005

559 Chen, S., Hamdi, R., Ochege, F. U., Du, H., Chen, X., Yang, W., & Zhang, C. (2019). Added Value of a
560 Dynamical Downscaling Approach for Simulating Precipitation and Temperature Over Tianshan
561 Mountains Area, Central Asia. *Journal of Geophysical Research: Atmospheres*, *124*(21), 11051–
562 11069. https://doi.org/10.1029/2019JD031016

563 Chen, X., Wei, W., & Liu, M. (2011). Change in fresh snow density in Tianshan Mountains, China.
564 *Chinese Geographical Science*, *21*(1), 36–47. https://doi.org/10.1007/s11769-010-0434-0

565 Chen, Y., Li, Z., Fang, G., & Li, W. (2018). Large Hydrological Processes Changes in the Transboundary
566 Rivers of Central Asia. *Journal of Geophysical Research: Atmospheres*, *123*, 5059–5069.
567 https://doi.org/10.1029/2017JD028184

568 Cohen, J., & Jones, J. (2011). A new index for more accurate winter predictions. *Geophysical Research*
569 *Letters*, *38*(21), 1–6. https://doi.org/10.1029/2011GL049626

570 Copernicus Climate Change Service: ERA5: Fifth generation of ECMWF atmospheric reanalyses of the
571 global climate, Coperni- cus Clim. Chang. Serv. Clim. Data Store, available at: https://cds.
572 climate.copernicus.eu/cdsapp#!/home (last access: 20 September 2005), 2017.

573 Dai, L., Che, T., Wang, J., & Zhang, P. (2012). Snow depth and snow water equivalent estimation from
574 AMSR-E data based on a priori snow characteristics in Xinjiang, China. *Remote Sensing of*
575 *Environment*, *127*, 14–29. https://doi.org/10.1016/j.rse.2011.08.029

576 Daloz, A. S., Mateling, M., L'Ecuyer, T., Kulie, M., Wood, N., Durand, M., et al. (2020). How much
577 snow falls in the world's mountains? A first look at mountain snowfall estimates in A-train
578 observations and reanalyses. *The Cryosphere*, *14*, 3195–3027.
579 https://doi.org/https://doi.org/10.5194/tc-14-3195-2020

580 Deng, J., Che, T., Xiao, C., Wang, S., Dai, L., & Meerzhan, A. (2019). Suitability analysis of ski areas in
581 China: An integrated study based on natural and socioeconomic conditions. *Cryosphere*, *13*(8),
582 2149–2167. https://doi.org/10.5194/tc-13-2149-2019

583 Dong, C. (2018). Remote sensing, hydrological modeling and in situ observations in snow cover research:
584 a review. *Journal of Hydrology*, *561*(April), 573–583.

https://doi.org/10.1016/j.jhydrol.2018.04.027

Dozier, J., Bair, E. H., & Davis, R. E. (2016). Estimating the spatial distribution of snow water equivalent in the world's mountains. *WIREs Water*, *3*(3), 461–474. https://doi.org/10.1002/wat2.1140

Dudhia, J. (1989). Numerical Study of Convection Observed during the Winter Monsoon Experiment Using a Mesoscale Two-Dimensional Model. *Journal of the Atmospheric Sciences*. https://doi.org/10.1175/1520-0469(1989)046<3077:NSOCOD>2.0.CO;2

ESA. Land Cover CCI Product User Guide Version 2. Tech. Rep. (2017). Available at: maps.elie.ucl.ac.be/CCI/viewer/download/ESACCI-LC-Ph2-PUGv2_2.0.pdf.

Fang, H., Baret, F., Plummer, S., & Schaepman-Strub, G. (2019). An Overview of Global Leaf Area Index (LAI): Methods, Products, Validation, and Applications. *Reviews of Geophysics*, *57*(3), 739–799. https://doi.org/10.1029/2018RG000608

Farinotti, D., Longuevergne, L., Moholdt, G., Duethmann, D., Mölg, T., Bolch, T., et al. (2015). Substantial glacier mass loss in the Tien Shan over the past 50 years. *Nature Geoscience*, *8*(9), 716–722. https://doi.org/10.1038/ngeo2513

Fernández-González, S., Valero, F., Sánchez, J. L., Gascón, E., López, L., García-Ortega, E., & Merino, A. (2015). Numerical simulations of snowfall events: Sensitivity analysis of physical parameterizations. *Journal of Geophysical Research*, *120*(19), 10130–10148. https://doi.org/10.1002/2015JD023793

Fiebrich, C. A., Morgan, Y. R., Mccombs, A. G., Hall, P. K., & Mcpherson, R. A. (2010). Quality assurance procedures for mesoscale meteorological data. *Journal of Atmospheric and Oceanic Technology*, *27*(10), 1565–1582. https://doi.org/10.1175/2010JTECHA1433.1

Gan, Y., Liang, X. Z., Duan, Q., Chen, F., Li, J., & Zhang, Y. (2019). Assessment and Reduction of the Physical Parameterization Uncertainty for Noah-MP Land Surface Model. *Water Resources Research*, *55*(7), 5518–5538. https://doi.org/10.1029/2019WR024814

Gerlitz, L., Steirou, E., Schneider, C., Moron, V., Vorogushyn, S., & Merz, B. (2019). Variability of the cold season climate in Central Asia. Part II: Hydroclimatic predictability. *Journal of Climate*, *32*(18), 6015–6033. https://doi.org/10.1175/JCLI-D-18-0892.1

612 Guo, L., & Li, L. (2015). Variation of the proportion of precipitation occurring as snow in the Tian Shan
613 Mountains, China. *International Journal of Climatology*, *35*(7), 1379–1393.
614 https://doi.org/10.1002/joc.4063

615 Hao, J., Huang, F., Liu, Y., & Li, L. (2018). Avalanche activity and characteristics of its triggering
616 factors in the western Tianshan Mountains , China. *Journal of Mountain Science*, *15*, 1397–1411.
617 https://doi.org/10.1007/s11629-018-4941-2

618 Hedstrom, N., & Pomeroy, J. W. (1998). Intercepted snow in the boreal forest: measurements and
619 modelling. *Hydrological Processes*, *12*(March), 1611–1625.

620 Helbig, N., Moeser, D., Teich, M., Vincent, L., Lejeune, Y., Sicart, J.-E., & Monnet, J.-M. (2019). Snow
621 processes in mountain forests: Interception modeling for coarse-scale applications. *Hydrology and*
622 *Earth System Sciences Discussions*, (August), 1–24. https://doi.org/10.5194/hess-2019-348

623 Hersbach, H., Bell, B., Berrisford, P., Hirahara, S., Horányi, A., Muñoz-Sabater, J., et al. (2020). The
624 ERA5 global reanalysis. *Quarterly Journal of the Royal Meteorological Society*, *146*(730), 1999–
625 2049. https://doi.org/10.1002/qj.3803

626 Holtzman, N. M., Pavelsky, T. M., Cohen, J. S., Wrzesien, M. L., & Herman, J. D. (2020). Tailoring
627 WRF and Noah-MP to Improve Process Representation of Sierra Nevada Runoff: Diagnostic
628 Evaluation and Applications. *Journal of Advances in Modeling Earth Systems*, *12*(3), 1–18.
629 https://doi.org/10.1029/2019MS001832

630 Hong, S., & Lim, J. (2006). The WRF single-moment 6-class microphysics scheme (WSM6). *Journal of*
631 *the Korean Meteorological Society*.

632 Hong, S. Y., Noh, Y., & Dudhia, J. (2006). A new vertical diffusion package with an explicit treatment of
633 entrainment processes. *Monthly Weather Review*, *134*(9), 2318–2341.
634 https://doi.org/10.1175/MWR3199.1

635 Huang, B., Hu, X., Fuglstad, G. A., Zhou, X., Zhao, W., & Cherubini, F. (2020). Predominant regional
636 biophysical cooling from recent land cover changes in Europe. *Nature Communications*, *11*(1), 1–
637 13. https://doi.org/10.1038/s41467-020-14890-0

638 Huning, L. S., & AghaKouchak, A. (2020). Global snow drought hot spots and characteristics.
639 *Proceedings of the National Academy of Sciences*, *117*(33), 19753–19759.

https://doi.org/10.1073/pnas.1915921117

Jiang, Y., Chen, F., Gao, Y., He, C., Barlage, M., & Huang, W. (2020). Assessment of uncertainty sources in snow cover simulations in the Tibetan Plateau. *Journal of Geophysical Research Atmospheres*, 125. https://doi.org/10.1029/2020JD032674

Jordan, R., 1991. A one-dimensional temperature model for a snow cover: Technical documentation for SNTHERM. 89 (No. CRREL-SR-91-16). Cold Regions Research and Engineering Lab Hanover NH.

Kain, J. S. (2004). The Kain–Fritsch Convective Parameterization: An Update. *Journal of Applied Meteorology*, *43*(1), 170–181. https://doi.org/10.1175/1520-0450(2004)043<0170:TKCPAU>2.0.CO;2

Kang, S., Zhang, Y., Qian, Y., & Wang, H. (2020). A review of black carbon in snow and ice and its impact on the cryosphere. *Earth-Science Reviews*, *210*, 103346. https://doi.org/10.1016/j.earscirev.2020.103346

Kendall, M.G., 1975. Rank Correlation Methods. Griffin, London.

de Kok, R. J., Kraaijenbrink, P. D. A., Tuinenburg, O. A., Bonekamp, P. N. J., & Immerzeel, W. W. (2020). Towards understanding the pattern of glacier mass balances in High Mountain Asia using regional climatic modelling. *The Cryosphere*, *14*(9), 3215–3234. https://doi.org/10.5194/tc-14-3215-2020

Kumar, S. V., M. Mocko, D., Wang, S., Peters-Lidard, C. D., & Borak, J. (2019). Assimilation of Remotely Sensed Leaf Area Index into the Noah-MP Land Surface Model: Impacts on Water and Carbon Fluxes and States over the Continental United States. *Journal of Hydrometeorology*, *20*(7), 1359–1377. https://doi.org/10.1175/jhm-d-18-0237.1

Landerer, F. W., & Swenson, S. C. (2012). Accuracy of scaled GRACE terrestrial water storage estimates. *Water Resources Research*, *48*(4), 1–11. https://doi.org/10.1029/2011WR011453

Li, J., Chen, F., Zhang, G., Barlage, M., Gan, Y., Xin, Y., & Wang, C. (2018). Impacts of Land Cover and Soil Texture Uncertainty on Land Model Simulations Over the Central Tibetan Plateau. *Journal of Advances in Modeling Earth Systems*, *10*(9), 2121–2146. https://doi.org/10.1029/2018MS001377

667 Li, Q., Yang, T., Zhang, F., Qi, Z., & Li, L. (2018). Snow depth reconstruction over last century: Trend
668 and distribution in the Tianshan Mountains, China. *Global and Planetary Change*, *173*(July 2018),
669 73–82. https://doi.org/10.1016/J.GLOPLACHA.2018.12.008

670 Li, Q., Yang, T., Zhou, H., & Li, L. (2019). Patterns in snow depth maximum and snow cover days
671 during 1961–2015 period in the Tianshan Mountains, Central Asia. *Atmospheric Research*,
672 *228*(April), 14–22. https://doi.org/10.1016/j.atmosres.2019.05.004

673 Lievens, H., Demuzere, M., Marshall, H. P., Reichle, R. H., Brucker, L., Brangers, I., et al. (2019). Snow
674 depth variability in the Northern Hemisphere mountains observed from space. *Nature*
675 *Communications*, *10*(1), 1–12. https://doi.org/10.1038/s41467-019-12566-y

676 Liu, L., Ma, Y., Menenti, M., Zhang, X., & Ma, W. (2019). Evaluation of WRF Modeling in Relation to
677 Different Land Surface Schemes and Initial and Boundary Conditions: A Snow Event Simulation
678 Over the Tibetan Plateau. *Journal of Geophysical Research: Atmospheres*, *124*(1), 209–226.
679 https://doi.org/10.1029/2018JD029208

680 Lu, H., Liu, M. Z., & Han, X. (2017). The effects of forest litter on snow energy budget in the Tianshan
681 Mountains, China. *Hydrological Processes*, *31*(8), 1602–1612. https://doi.org/10.1002/hyp.11129

682 Luo, Y., Arnold, J., Liu, S., Wang, X., & Chen, X. (2013). Inclusion of glacier processes for distributed
683 hydrological modeling at basin scale with application to a watershed in Tianshan Mountains,
684 northwest China. *Journal of Hydrology*, *477*, 72–85. https://doi.org/10.1016/j.jhydrol.2012.11.005

685 Ma, N., Yu, K., Zhang, Y., Zhai, J., Zhang, Y., & Zhang, H. (2020). Ground observed climatology and
686 trend in snow cover phenology across China with consideration of snow-free breaks. *Climate*
687 *Dynamics*, *55*(9–10), 2867–2887. https://doi.org/10.1007/s00382-020-05422-z

688 Ma, X., Jin, J., Liu, J., & Niu, G.-Y. (2019). An improved vegetation emissivity scheme for land surface
689 modeling and its impact on snow cover simulations. *Climate Dynamics*, (0123456789).
690 https://doi.org/10.1007/s00382-019-04924-9

691 Mann, H.B., 1945. Nonparametric tests against trend. Econometrica 13, 245–259.

692 Mazurkiewicz, A. B., Callery, D. G., & McDonnell, J. J. (2008). Assessing the controls of the snow
693 energy balance and water available for runoff in a rain-on-snow environment. *Journal of*
694 *Hydrology*, *354*(1–4), 1–14. https://doi.org/10.1016/j.jhydrol.2007.12.027

695 Minder, J. R., Letcher, T. W., & Skiles, S. M. K. (2016). An evaluation of high-resolution regional
696 climate model simulations of snow cover and albedo over the rocky mountains, with implications
697 for the simulated snow-albedo feedback. *Journal of Geophysical Research*, *121*(15), 9069–9088.
698 https://doi.org/10.1002/2016JD024995

699 Mlawer, E. J., Taubman, S. J., Brown, P. D., Iacono, M. J., & Clough, S. A. (1997). Radiative transfer for
700 inhomogeneous atmospheres: RRTM, a validated correlated-k model for the longwave. *Journal of*
701 *Geophysical Research*, *102*(D14), 16663. https://doi.org/10.1029/97JD00237

702 Mölg, T., Maussion, F., & Scherer, D. (2014). Mid-latitude westerlies as a driver of glacier variability in
703 monsoonal High Asia. *Nature Climate Change*, *4*(1), 68–73. https://doi.org/10.1038/nclimate2055

704 Monin, A. S., & Obukhov, A. M. (1959). Basic laws of turbulent mixing in the surface layer of the
705 atmosphere. *Tr Akad Nauk SSSR Geofiz Inst*, *24*(151), 163–187.

706 Mortimer, C., Mudryk, L., Derksen, C., Luojus, K., Brown, R., Kelly, R., & Tedesco, M. (2020).
707 Evaluation of long-term Northern Hemisphere snow water equivalent products. *The Cryosphere*,
708 *14*(5), 1579–1594. https://doi.org/10.5194/tc-14-1579-2020

709 Mudryk, L. R., Derksen, C., Kushner, P. J., & Brown, R. (2015). Characterization of Northern
710 Hemisphere snow water equivalent datasets, 1981-2010. *Journal of Climate*, *28*(20), 8037–8051.
711 https://doi.org/10.1175/JCLI-D-15-0229.1

712 Musselman, K. N., Lehner, F., Ikeda, K., Clark, M. P., Prein, A. F., Liu, C., et al. (2018). Projected
713 increases and shifts in rain-on-snow flood risk over western North America. *Nature Climate*
714 *Change*, *8*(9), 808–812. https://doi.org/10.1038/s41558-018-0236-4

715 Niu, G. Y., & Yang, Z. L. (2004). Effects of vegetation canopy processes on snow surface energy and
716 mass balances. *Journal of Geophysical Research: Atmospheres*, *109*(23), 1–15.
717 https://doi.org/10.1029/2004JD004884

718 Niu, G. Y., Yang, Z. L., Mitchell, K. E., Chen, F., Ek, M. B., Barlage, M., et al. (2011). The community
719 Noah land surface model with multiparameterization options (Noah-MP): 1. Model description
720 and evaluation with local-scale measurements. *Journal of Geophysical Research Atmospheres*,
721 *116*(12), 1–19. https://doi.org/10.1029/2010JD015139

722 Nogueira, M. (2020). Inter-comparison of ERA-5, ERA-interim and GPCP rainfall over the last 40 years:

Process-based analysis of systematic and random differences. *Journal of Hydrology*, *583*, 124632. https://doi.org/10.1016/j.jhydrol.2020.124632

Norris, J., Carvalho, L. M. V., Jones, C., & Cannon, F. (2015). WRF simulations of two extreme snowfall events associated with contrasting extratropical cyclones over the western and central Himalaya. *Journal of Geophysical Research*, *120*(8), 3114–3138. https://doi.org/10.1002/2014JD022592

Norris, Jesse, Carvalho, L. M. V., Jones, C., & Cannon, F. (2018). Deciphering the contrasting climatic trends between the central Himalaya and Karakoram with 36 years of WRF simulations. *Climate Dynamics*, *0*(0), 1–22. https://doi.org/10.1007/s00382-018-4133-3

Notarnicola, C. (2020). Hotspots of snow cover changes in global mountain regions over 2000–2018. *Remote Sensing of Environment*, *243*(June 2019), 111781. https://doi.org/10.1016/j.rse.2020.111781

Oaida, C. M., Xue, Y., Flanner, M. G., Skiles, S. M. K., De Sales, F., & Painter, T. H. (2015). Improving snow albedo processes in WRF/SSiB regional climate model to assess impact of dust and black carbon in snow on surface energy balance and hydrology over western U.S. *Journal of Geophysical Research*, *120*(8), 3228–3248. https://doi.org/10.1002/2014JD022444

Orsolini, Y., Wegmann, M., Dutra, E., Liu, B., Balsamo, G., Yang, K., et al. (2019). Evaluation of snow depth and snow cover over the Tibetan Plateau in global reanalyses using in situ and satellite remote sensing observations. *The Cryosphere*, *13*(8), 2221–2239. https://doi.org/10.5194/tc-13-2221-2019

Ou, T., Chen, D., Chen, X., Lin, C., Yang, K., Lai, H. W., & Zhang, F. (2020). Simulation of summer precipitation diurnal cycles over the Tibetan Plateau at the gray-zone grid spacing for cumulus parameterization. *Climate Dynamics*, *54*(7–8), 3525–3539. https://doi.org/10.1007/s00382-020-05181-x

Peng, S., Piao, S., CIAIS, P., Fang, J., & Wang, X. (2010). Change in winter snow depth and its impacts on vegetation in China. *Global Change Biology*, *16*(11), 3004–3013. https://doi.org/10.1111/j.1365-2486.2010.02210.x

Piao, S., Wang, X., Park, T., Chen, C., Lian, X., He, Y., et al. (2020). Characteristics, drivers and feedbacks of global greening. *Nature Reviews Earth & Environment*, *1*(1), 14–27.

https://doi.org/10.1038/s43017-019-0001-x

Pritchard, D. M. W., Forsythe, N., O'Donnell, G., Fowler, H. J., & Rutter, N. (2020). Multi-physics ensemble snow modelling in the western Himalaya. *Cryosphere*, *14*(4), 1225–1244. https://doi.org/10.5194/tc-14-1225-2020

Pulliainen, J., Luojus, K., Derksen, C., Mudryk, L., Lemmetyinen, J., Salminen, M., et al. (2020). Patterns and trends of Northern Hemisphere snow mass from 1980 to 2018. *Nature*, *581*(7808), 294–298. https://doi.org/10.1038/s41586-020-2258-0

Qin, Y., Abatzoglou, J. T., Siebert, S., Huning, L. S., AghaKouchak, A., Mankin, J. S., et al. (2020). Agricultural risks from changing snowmelt. *Nature Climate Change*, *10*(5), 459–465. https://doi.org/10.1038/s41558-020-0746-8

Ryken, A., Bearup, L. A., Jefferson, J. L., Constantine, P., & Maxwell, R. M. (2020). Sensitivity and model reduction of simulated snow processes: Contrasting observational and parameter uncertainty to improve prediction. *Advances in Water Resources*, *135*(September 2019), 103473. https://doi.org/10.1016/j.advwatres.2019.103473

Sarangi, C., Qian, Y., Rittger, K., Leung, L. R., Chand, D., Bormann, K. J., & Painter, T. H. (2020). Dust dominates high-altitude snow darkening and melt over high-mountain Asia. *Nature Climate Change*. https://doi.org/10.1038/s41558-020-00909-3

Schweizer, J., Jamieson, J. B., & Schneebeli, M. (2003). Snow avalanche formation. *Reviews of Geophysics*, *41*(4). https://doi.org/10.1029/2002RG000123

Sen, P. K. (1968). Journal of the American Statistical Estimates of the Regression Coefficient Based on Kendall's Tau. *Journal of the Americal Statistical Association*, *63*(324), 1379–1389. https://doi.org/10.1080/ 01621459.1968.10480934

Skamarock, William C., Klemp, Joseph B., 2008. A time-split nonhydrostatic atmospheric model for weather research and forecasting applications. J. Comput. Phys. 227 (7), 3465–3485.

Smith, T., & Bookhagen, B. (2016). Assessing uncertainty and sensor biases in passive microwave data across High Mountain Asia. *Remote Sensing of Environment*, *181*, 174–185. https://doi.org/10.1016/j.rse.2016.03.037

778 Smith, T., & Bookhagen, B. (2018). Changes in seasonal snow water equivalent distribution in high
779 mountain Asia (1987 to 2009). *Science Advances*, *4*(1). https://doi.org/10.1126/sciadv.1701550

780 Sorg, A., Bolch, T., Stoffel, M., Solomina, O., & Beniston, M. (2012). Climate change impacts on
781 glaciers and runoff in Tien Shan (Central Asia). *Nature Climate Change*, *2*(10), 725–731.
782 https://doi.org/10.1038/nclimate1592

783 Stewart, I. T. (2010). Changes in snowpack and snowmelt runoff for key mountain regions. *Hydrological*
784 *Processes*, *23*, 78–94. https://doi.org/10.1002/hyp.7128

785 Takala, M., Luojus, K., Pulliainen, J., Derksen, C., Lemmetyinen, J., Kärnä, J. P., et al. (2011).
786 Estimating northern hemisphere snow water equivalent for climate research through assimilation
787 of space-borne radiometer data and ground-based measurements. *Remote Sensing of Environment*,
788 *115*(12), 3517–3529. https://doi.org/10.1016/j.rse.2011.08.014

789 Terzago, S., Andreoli, V., Arduini, G., Balsamo, G., Campo, L., Cassardo, C., et al. (2020). Sensitivity of
790 snow models to the accuracy of meteorological forcings in mountain environment. *Hydrology and*
791 *Earth System Sciences*, *24*, 4061–4090. https://doi.org/https://doi.org/10.5194/hess-24-4061-2020

792 Tomasi, E., Giovannini, L., Zardi, D., & de Franceschi, M. (2017). Optimization of Noah and Noah_MP
793 WRF Land Surface Schemes in Snow-Melting Conditions over Complex Terrain. *Monthly*
794 *Weather Review*, *145*(12), 4727–4745. https://doi.org/10.1175/MWR-D-16-0408.1

795 Tomaszewska, M. A., & Henebry, G. M. (2018). Changing snow seasonality in the highlands of
796 Kyrgyzstan. *Environmental Research Letters*, *13*(6). https://doi.org/10.1088/1748-9326/aabd6f

797 Tomaszewska, M. A., Nguyen, L. H., & Henebry, G. M. (2020). Land surface phenology in the highland
798 pastures of montane Central Asia: Interactions with snow cover seasonality and terrain
799 characteristics. *Remote Sensing of Environment*, *240*(January), 111675.
800 https://doi.org/10.1016/j.rse.2020.111675

801 Unger-Shayesteh, K., Vorogushyn, S., Farinotti, D., Gafurov, A., Duethmann, D., Mandychev, A., &
802 Merz, B. (2013). What do we know about past changes in the water cycle of Central Asian
803 headwaters? A review. *Global and Planetary Change*, *110*, 4–25.
804 https://doi.org/10.1016/j.gloplacha.2013.02.004

805 Wang, C., Graham, R. M., Wang, K., Gerland, S., & Granskog, M. A. (2019). Comparison of ERA5 and

ERA-Interim near surface air temperature and precipitation over Arctic sea ice: Effects on sea ice thermodynamics and evolution. *The Cryosphere*, *13*, 1661–1679. https://doi.org/https://doi.org/10.5194/tc-13-1661-2019

Wang, W., Yang, K., Zhao, L., Zheng, Z., Lu, H., & Mamtimin, A. (2020). Characterizing surface albedo of shallow fresh snow and its importance for snow ablation on the interior of the Tibetan Plateau. *Journal of Hydrometeorology*, *21*, 815–827. https://doi.org/10.1175/JHM-D-19-0193.1.

Wang, X., Wu, C., Peng, D., Gonsamo, A., & Liu, Z. (2018). Snow cover phenology affects alpine vegetation growth dynamics on the Tibetan Plateau: Satellite observed evidence, impacts of different biomes, and climate drivers. *Agricultural and Forest Meteorology*, *256–257*(May 2017), 61–74. https://doi.org/10.1016/j.agrformet.2018.03.004

Wang, Yan, Xie, Z., Jia, B., Wang, L., Li, R., Liu, B., et al. (2020). Sensitivity of Snow Simulations to Different Atmospheric Forcing Data Sets in the Land Surface Model CAS-LSM. *Journal of Geophysical Research: Atmospheres*, *125*(16), 1–24. https://doi.org/10.1029/2019JD032001

Wang, Yan, Yang, K., Zhou, X., Chen, D., Lu, H., Ouyang, L., et al. (2020). Synergy of orographic drag parameterization and high resolution greatly reduces biases of WRF-simulated precipitation in central Himalaya. *Climate Dynamics*, *54*(3–4), 1729–1740. https://doi.org/10.1007/s00382-019-05080-w

Wang, Yuanheng, Broxton, P., Fang, Y., Behrangi, A., Barlage, M., Zeng, X., & Niu, G. (2019). A Wet-Bulb Temperature-Based Rain-Snow Partitioning Scheme Improves Snowpack Prediction Over the Drier Western United States. *Geophysical Research Letters*, *46*(23), 13825–13835. https://doi.org/10.1029/2019GL085722

Wrzesien, M. L., Durand, M. T., Pavelsky, T. M., Howat, I. M., Margulis, S. A., & Huning, L. S. (2017). Comparison of methods to estimate snow water equivalent at the mountain range scale: A case study of the California Sierra Nevada. *Journal of Hydrometeorology*, *18*(4), 1101–1119. https://doi.org/10.1175/JHM-D-16-0246.1

Wrzesien, M. L., Durand, M. T., Pavelsky, T. M., Kapnick, S. B., Zhang, Y., Guo, J., & Shum, C. K. (2018). A New Estimate of North American Mountain Snow Accumulation From Regional Climate Model Simulations. *Geophysical Research Letters*, *45*(3), 1423–1432.

https://doi.org/10.1002/2017GL076664

Wrzesien, M. L., Pavelsky, T. M., Durand, M. T., Dozier, J., & Lundquist, J. D. (2019). Characterizing Biases in Mountain Snow Accumulation From Global Data Sets. *Water Resources Research*, *55*(11), 9873–9891. https://doi.org/10.1029/2019WR025350

Xiao, Z., Liang, S., Wang, J., Chen, P., Yin, X., Zhang, L., & Song, J. (2014). Use of general regression neural networks for generating the GLASS leaf area index product from time-series MODIS surface reflectance. *IEEE Transactions on Geoscience and Remote Sensing*, *52*(1), 209–223. https://doi.org/10.1109/TGRS.2013.2237780

Xiao, Z., Liang, S., Wang, J., Xiang, Y., Zhao, X., & Song, J. (2016). Long-Time-Series Global Land Surface Satellite Leaf Area Index Product Derived from MODIS and AVHRR Surface Reflectance. *IEEE Transactions on Geoscience and Remote Sensing*, *54*(9), 5301–5318. https://doi.org/10.1109/TGRS.2016.2560522

Yang, J., Jiang, L., Luojus, K., Pan, J., Lemmetyinen, J., Takala, M., & Wu, S. (2020). Real-Time Snow Depth Estimation and Historical Data Reconstruction Over China Based on a Random Forest Machine Learning Approach. *The Cryosphere*, *14*, 1763–1778. https://doi.org/https://doi.org/10.5194/tc-14-1763-2020

Yang, J. W., Jiang, L., Lemmetyinen, J., Luojus, K., Takala, M., Wu, S., & Pan, J. (2020). Validation of remotely sensed estimates of snow water equivalent using multiple reference datasets from the middle and high latitudes of China. *Journal of Hydrology*, *590*, 125499. https://doi.org/10.1016/j.jhydrol.2020.125499

Yang, R., Friedl, M. A., & Ni, W. (2001). Parameterization of shortwave radiation fluxes for nonuniform vegetation canopies in land surface models. *Journal of Geophysical Research : Atmospheres*, *106(D13)*, 14,245-14,286.

Yang, T., Li, Q., Ahmad, S., Zhou, H., & Li, L. (2019). Changes in Snow Phenology from 1979 to 2016 over the Tianshan Mountains, Central Asia. *Remote Sensing*, *11*(5), 499. https://doi.org/10.3390/rs11050499

Yang, T., Li, Q., Liu, W., Liu, X., Li, L., & De Maeyer, P. (2019). Spatiotemporal variability of snowfall and its concentration in northern Xinjiang, Northwest China. *Theoretical and Applied Climatology*,

1–13. https://doi.org/10.1007/s00704-019-02994-7

Yang, T., Li, Q., Chen, X., Hamdi, R., Maeyer, P. De, Kurban, A., & Li, L. (2020). Improving snow simulation with more realistic vegetation parameters in a regional climate model in the Tianshan Mountains , Central Asia. *Journal of Hydrology*, *590*, 125525. https://doi.org/10.1016/j.jhydrol.2020.125525

Ye, K. (2019). Interannual variability of March snow mass over Northern Eurasia and its relation to the concurrent and preceding surface air temperature, precipitation and atmospheric circulation. *Climate Dynamics*, *52*(5–6), 2813–2836. https://doi.org/10.1007/s00382-018-4297-x

You, Y., Huang, C., Yang, Z., Zhang, Y., Bai, Y., & Gu, J. (2020). Assessing Noah-MP parameterization sensitivity and uncertainty interval across snow climates. *Journal of Geophysical Research: Atmospheres*, 1–20. https://doi.org/10.1029/2019jd030417

You, Y., Huang, C., Gu, J., Li, H., Hao, X., & Hou, J. (2020). Assessing snow simulation performance of typical combination schemes within Noah-MP in northern Xinjiang, China. *Journal of Hydrology*, *581*(November 2019), 124380. https://doi.org/10.1016/j.jhydrol.2019.124380

Zhang, T. (2005). Influence of the seasonal snow cover on the ground thermal regime: An overview. *Reviews of Geophysics*, *43*, RG4002. https://doi.org/doi:10.1029/2004RG000157.

Zhao, C., Yang, Y., Fan, H., Huang, J., Fu, Y., Zhang, X., et al. (2020). Aerosol characteristics and impacts on weather and climate over the Tibetan Plateau. *National Science Review*, *7*(3), 492–495. https://doi.org/10.1093/nsr/nwz184

Zhong, X., Zhang, T., Kang, S., Wang, K., Zheng, L., Hu, Y., & Wang, H. (2018). Spatiotemporal variability of snow depth across the Eurasian continent from 1966 to 2012. *Cryosphere*, *12*(1), 227–245. https://doi.org/10.5194/tc-12-227-2018

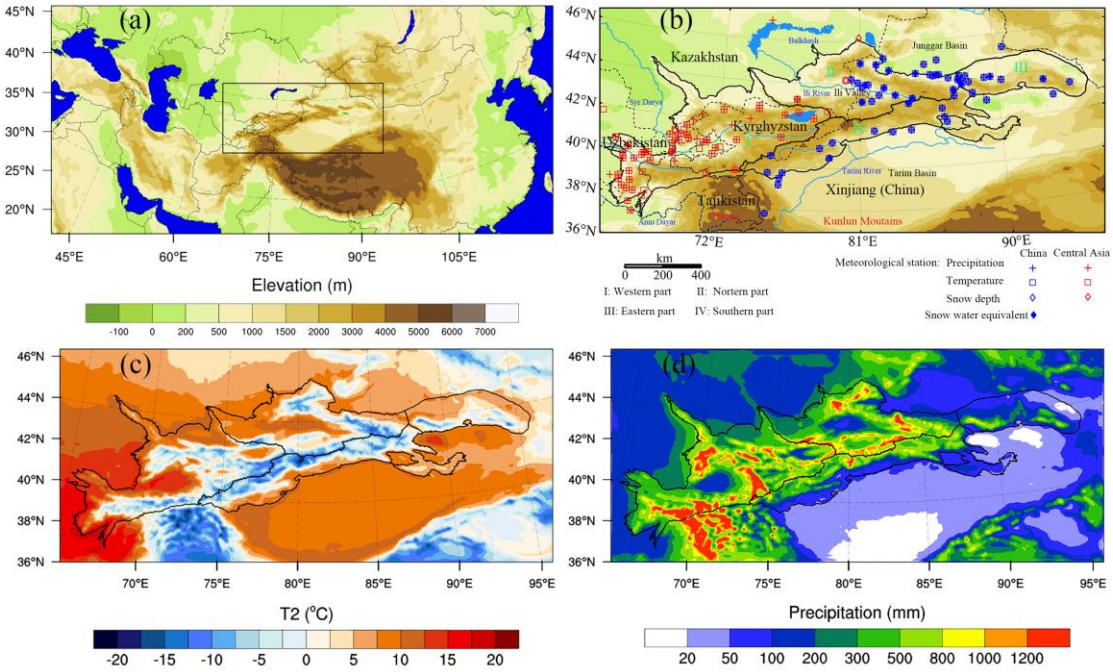

884

885 **Figure 1** Topography (m) of the model domains (a); Location of the TS (b), Mean annual temperature

886 (c) and precipitation (d) from the WRF model.

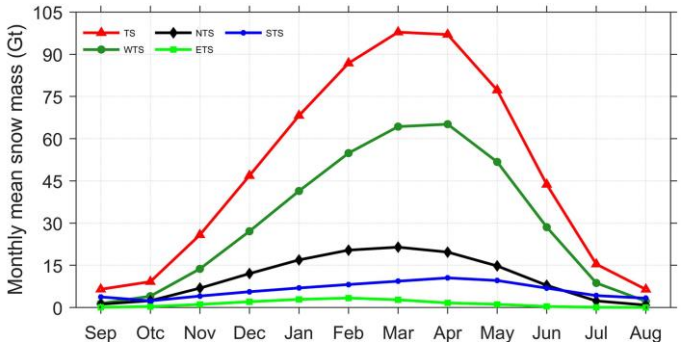

887

888 **Figure 2** Annual variation of the monthly snow mass from D02 in the TS and its sub-regions.

889

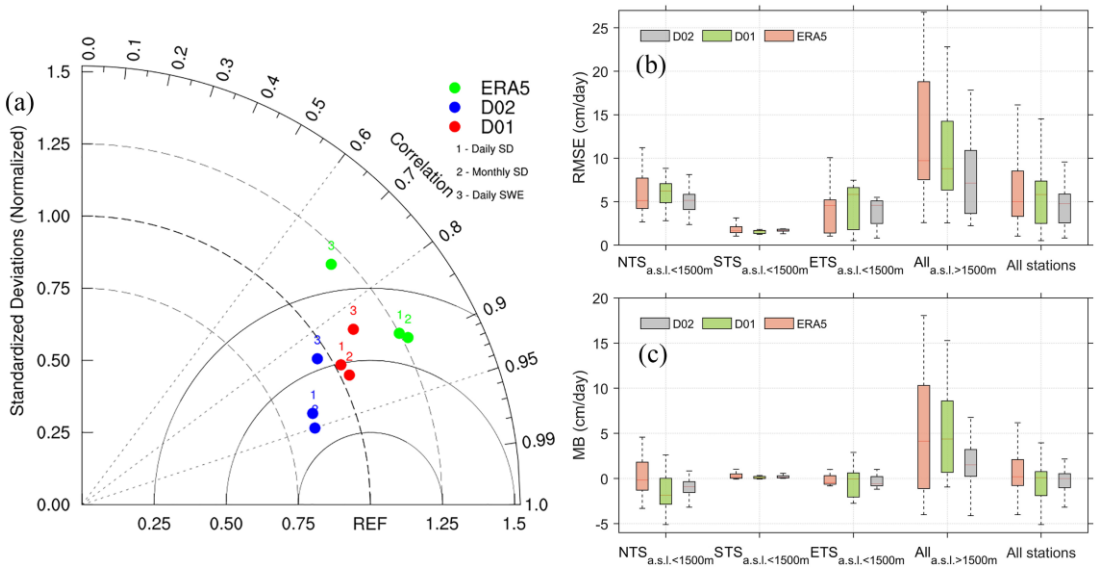

Figure 3 Taylor diagram comparing the in-situ SD and SWE with different simulations for the average from all stations in the TS on daily and monthly time scales (a). Values closer to the reference point indicate a higher correlation and smaller differences invariance. Boxplot of the root mean square error (cm/day) (b) and mean bias (cm/day) (c) of different daily SD simulations in the sub-regions. The bottom and top edges of each box indicate the 25th and 75th percentile and the central line indicates the median.

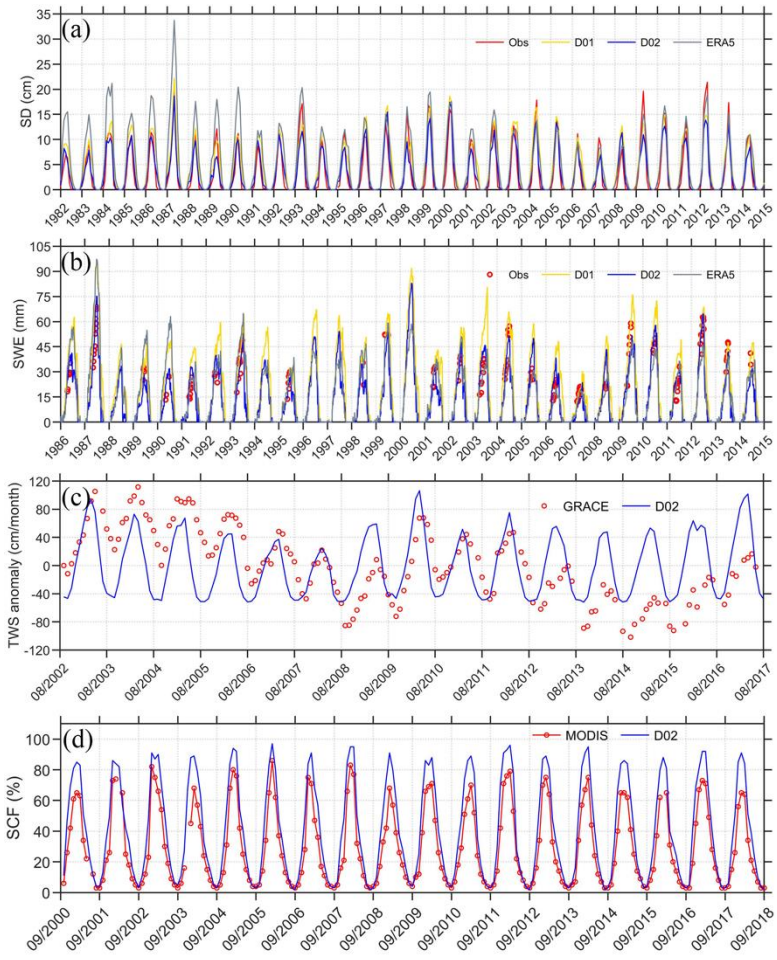

897

898 **Figure 4** Comparison of the time series observations and simulations of the monthly SD (a) and daily
899 SWE (b) averages from all stations. (c) Monthly TWS anomaly estimated by D02 in comparison with
900 GRACE. (d) Mean monthly SFC estimated by D02 in comparison with the MODIS values.

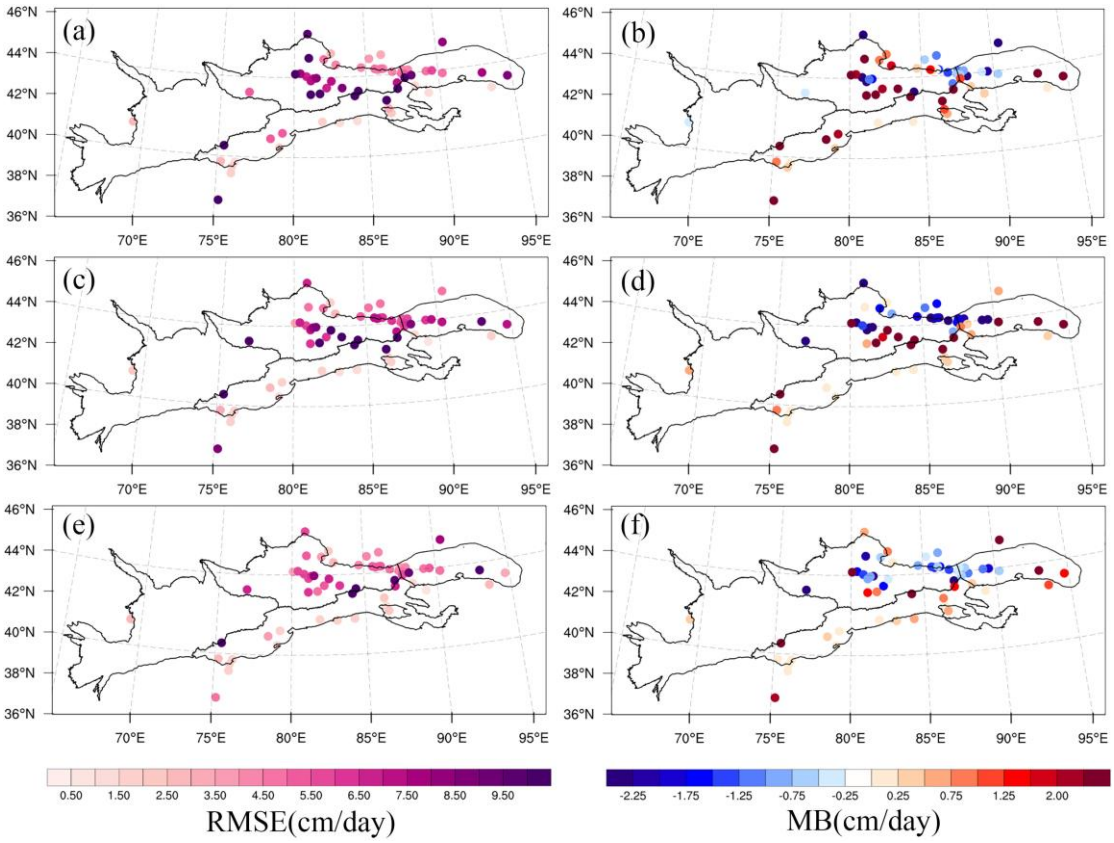

Figure 5 Spatial distribution of the RMSE (left panels, cm/day) and MB (right panels, cm/day) between the daily estimated SD (ERA5 (a and b), D01(c and d) and D02 (e and f)) and the observations.

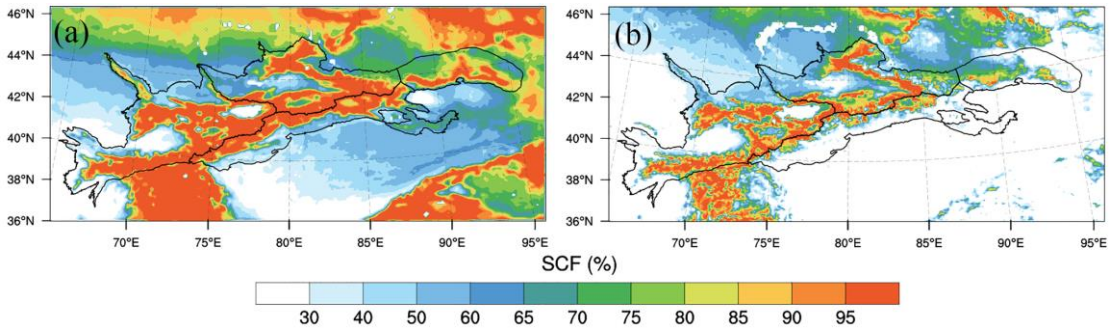

Figure 6 Spatial distribution of the (a) estimated SCF and (b) MODIS SFC during the cold season.

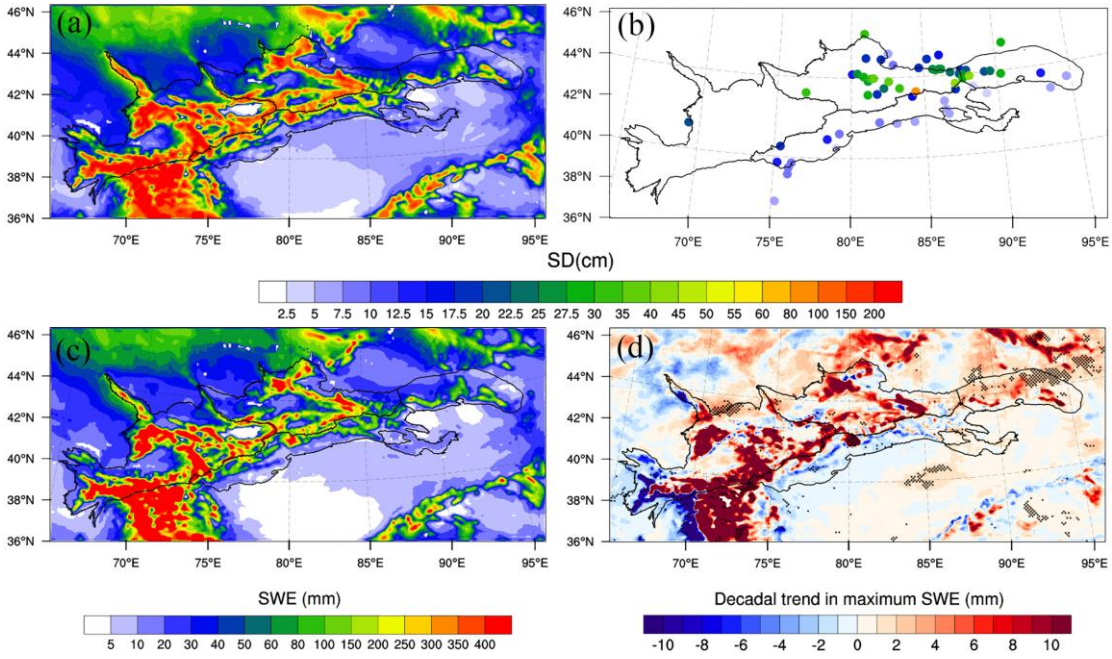

908

909 **Figure 7** Climatology of the estimated maximum SD (a), observed SD (b), and estimated maximum

910 SWE (c) during the cold season. Trend of the maximum SWE (d). The black dots in Figure 7 indicate

911 significant trends (significance level at 0.05).

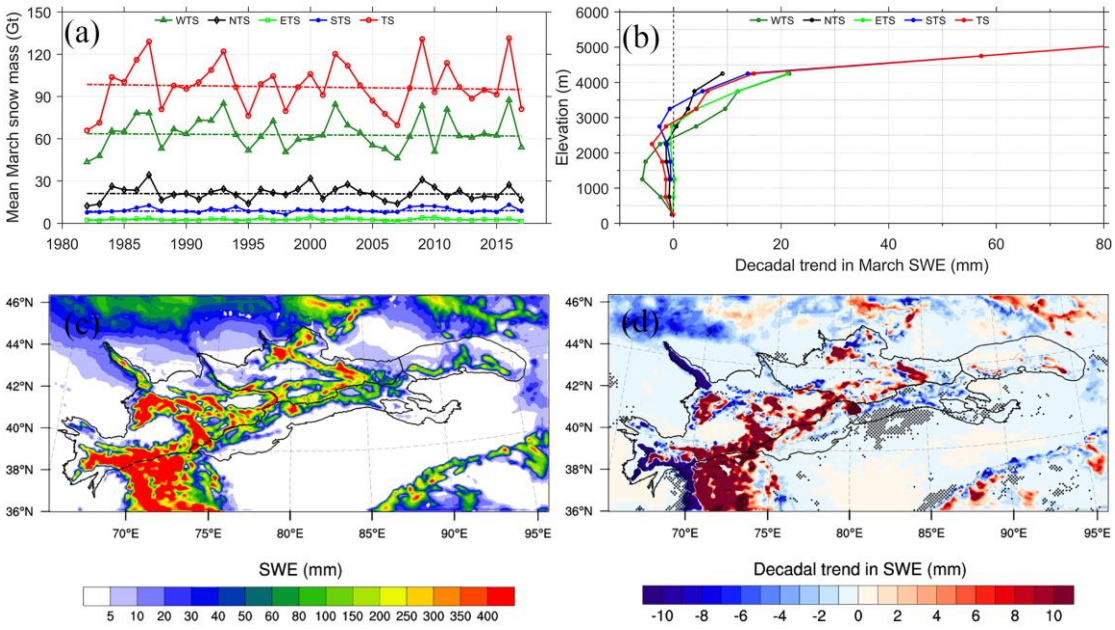

912

913 **Figure 8** Variation of the March snow mass (a) and elevation variation in the decadal trend for the

914 March SWE (b). Climatology of the March SWE (c) and its trend (d) in the TS. The black dots in

915 Figures 8 c and 8d indicate significant trends (significance level at 0.05).

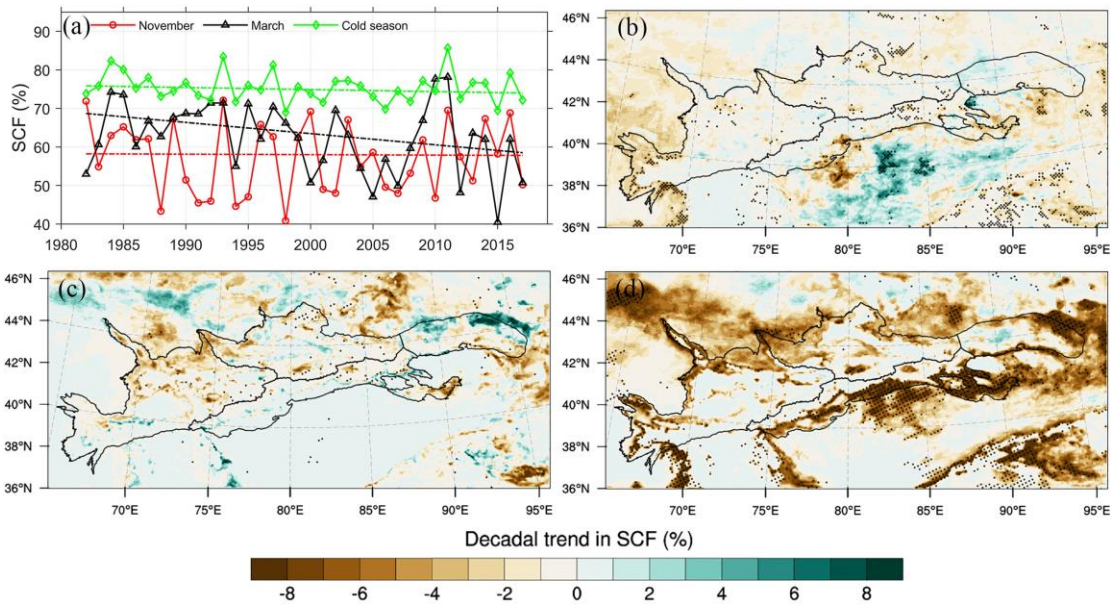

Figure 9 Variations of (a) the mean SFC in the TS. Spatial trends of (b) the cold season, (c) November, and (d) March in the mean SCF. The black dots in Figure 9 indicate significant trends (significance level at 0.05).

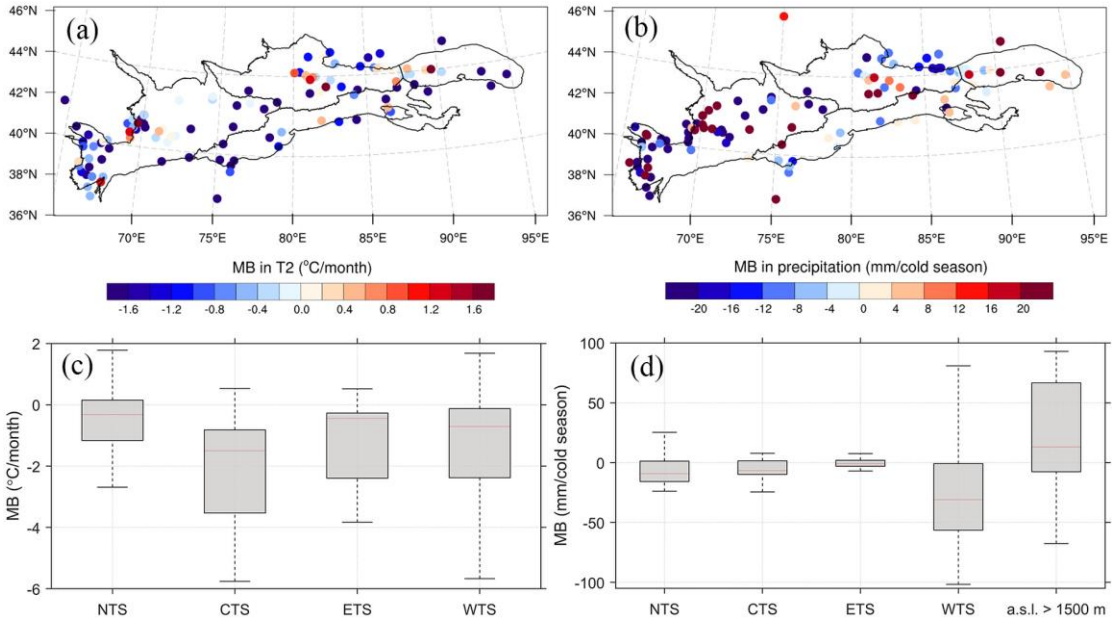

Figure 10 Spatial distribution of the mean bias between the simulations and in-situ observations in (a) the mean monthly temperature (°C/month) and (b) total cold season precipitation (mm/cold season). Boxplot of the (c) mean monthly temperature bias and (d) total cold season precipitation bias in the different sub-regions. The bottom and top edges of each box indicate the 25th and 75th percentile and the central line indicates the median.

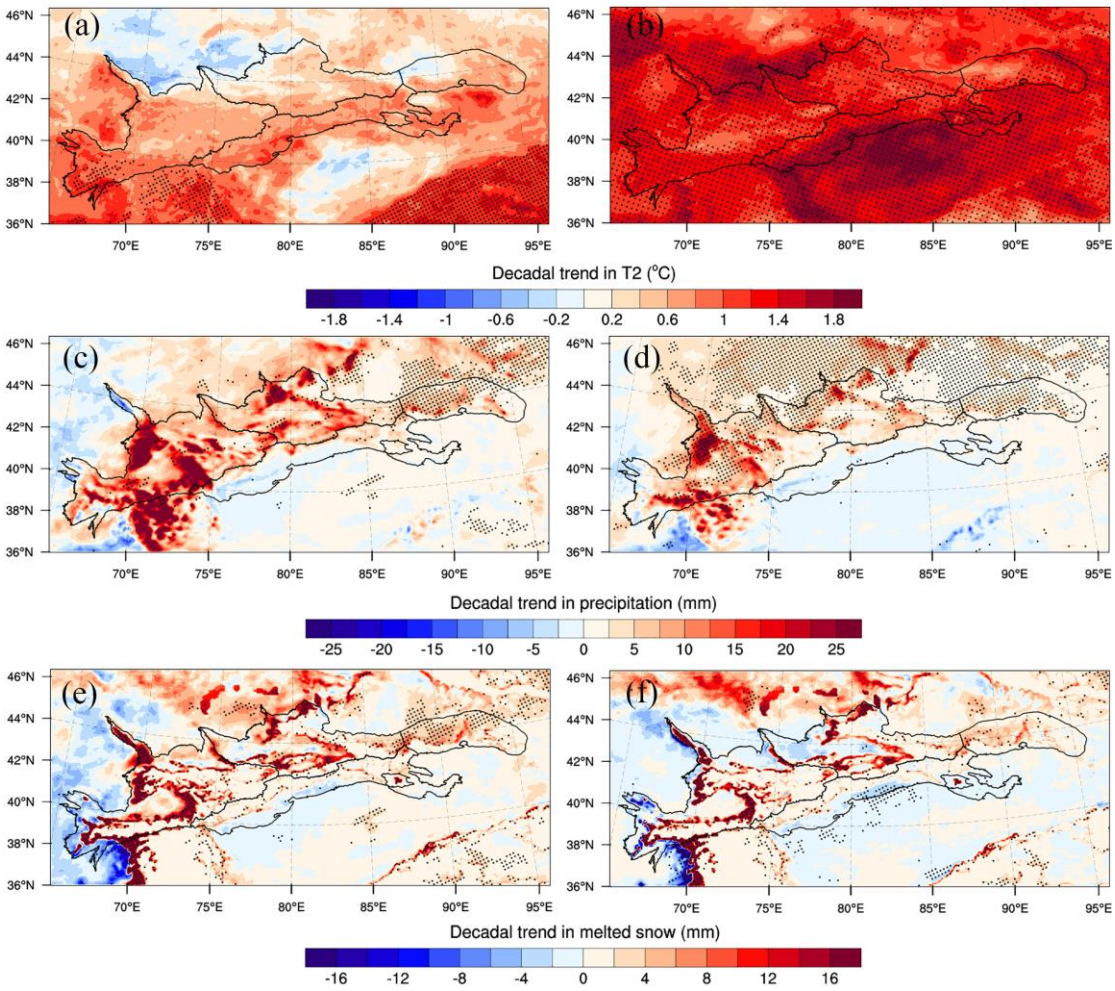

Figure 11 Cold season (left panels) and March trends (right panels) regarding the mean temperature (a and b), total precipitation (c and d), and melted snow (e and f). The black dots in Figure 9 indicate that the trends are significant (significance level at 0.05).

940 **Table 1** Information on the validation dataset.

Dataset name	Variables (resolution)	Period	Data sources
CMA V3.0	TP, T2, SD, and SWE	1982/10/01-2015/09/30	http://data.cma.cn/
TSSAR	TP,T2, SD and SWE	1982/10/01-2015/09/30	Chinese Academy of Sciences
Central Asia	TP and T2	1982/10-2000/12	https://nsidc.org/data/G02174
Former USSR	SD	1982/10/01-2015/09/30	http://aisori.meteo.ru/ClimateR
GRACE TWS	TWS (0.5°×0.5°)	2002/09-2017/09	https://grace.jpl.nasa.gov/data/
MOD10CM	SCF (0.05°×0.05°)	2000/09-2018/09	https://urs.earthdata.nasa.gov/

941 TP, T2, SD, SWE TWS, and SCF represent the total precipitation, air temperature at 2m, snow depth,
942 snow water equivalent, and Terrestrial Water Storage, respectively.

943

944 **Table 2** Main physical parameterizations used in the numerical simulation.

Simulation period	1982-10-01 to 2018-09-30
Model Version:	Version 4.01
Nest:	2
Horizontal grid (D02):	9 km
Number of grids:	304*133
Vertical Levels:	35
Microphysics' scheme:	WSM-6
Longwave radiation scheme:	RRTM
Shortwave radiation scheme:	Dudhia
Surface layer:	Revised MM5 Monin-Obukhov
Planetary boundary layer:	YSU
Cumulus parameterization:	Kain-Fritsch
Initial/lateral boundary condition:	ERA5
Land cover:	CCI-2000
Land surface model:	Noah-MP

945

Table 3 The correlation coefficient, MB, and RMSE of the monthly TWS anomaly and SCF between the D02 and satellite observations (GRACE and MODIS) in the TS during the cold season.

	R	MB (mm or %/month)	RMSE (mm or %/month)
TWS	0.43**	21.70 mm	51.10 mm
SCF	0.98**	11.28%	14.42%

** Significant at the 0.01 level.

Table 4 The decadal variation of SCF (%) in the TS and its sub-regions.

	WTS	NTS	ETS	STS	TS
cold season	-0.94	-0.24	-0.16	-0.86	-0.53
November	-1.37	-0.29	0.48	0.98	-0.12
March	-2.70	-1.84	-2.86	-4.90*	2.91*

* Significant at the 0.05 level.

Table 5 Pearson's R values for the correlations between the March snow mass, SCF and the melted snow and March T2 and total precipitation in the TS during the cold season.

	March snow mass	March SCF	March melted snow
March T2	-0.22	-0.91**	0.49**
Cold precipitation	0.78**	-0.05	0.28

**Significant at the 0.01 level.